Geochemistry, Geophysics, Geosystems

RESEARCH ARTICLE
10.1029/2020GC008953

Seismicity of the Incoming Plate and Forearc Near the Mariana Trench Recorded by Ocean Bottom Seismographs

Melody Eimer[1], Douglas A. Wiens[1], Chen Cai[1,2], Daniel Lizarralde[3], and Hope Jasperson[1,4]

[1]Department of Earth and Planetary Sciences, Washington University in Saint Louis, St. Louis, MO, USA, [2]School of Earth Sciences and EngineeringSun-Yat Sen University, Guangzhou, China, [3]Department of Geology and Geophysics, Woods Hole Oceanographic Institution, Woods Hole, MA, USA, [4]Earth, Environmental and Planetary Sciences, Rice University, Houston, TX, USA

Abstract Earthquakes near oceanic trenches are important for studying incoming plate bending and updip thrust zone seismogenesis, yet are poorly constrained using seismographs on land. We use an ocean bottom seismograph (OBS) deployment spanning both the incoming Pacific Plate and the forearc to study seismicity near the Mariana Trench. The yearlong deployment in 2012–2013 consisted of 20 broadband OBSs and 5 suspended hydrophones, with an additional 59 short period OBSs and hydrophones recording for 1 month. We locate 1,692 earthquakes using a nonlinear method with a 3D velocity model constructed from active source profiles and surface wave tomography results. Events occurring seaward of the trench occur to depths of ~35 km below the seafloor, and focal mechanisms of the larger events indicate normal faulting corresponding to plate bending. Significant seismicity emerges about 70 km seaward from the trench, and the seismicity rate increases continuously towards the trench, indicating that the largest bending deformation occurs near the trench axis. These plate-bending earthquakes occur along faults that facilitate the hydration of the subducting plate, and the lateral and depth distribution of earthquakes is consistent with low-velocity regions imaged in previous studies. The forearc is marked by a heterogeneous distribution of low magnitude (<5 M_w) thrust zone seismicity, possibly due to the rough incoming plate topography and/or serpentinization of the forearc. A sequence of thrust earthquakes occurs at depths ~10 km below seafloor and within 20 km of the trench axis, demonstrating that the megathrust is seismically active nearly to the trench.

Plain Language Summary Studying earthquakes near oceanic trenches is important for understanding subduction zones but can be difficult using only distant land-based instruments. This study uses seismographs designed to work on the seafloor to study earthquakes near the central Mariana Trench. As the subducting plate bends, faults form due to the increased extensional stress. These faults can become pathways for water to penetrate into this subducting plate. Understanding the amount of water stored in the plate is essential for constraining the global water cycle, and the earthquake distribution allows us to determine the distribution of active faults. We found that the earthquakes occur shallower than 35-km depth and within 70 km seaward of the trench. We also study earthquakes occurring along the megathrust, which is the interface between the subducting plate and the overriding plate that is prone to seismic activity. We found that the earthquakes show a patchy distribution, indicating that the megathrust interface is not uniform. This could be related to topographic features on the subducting plate interacting with the plate above. We also observed earthquakes at depths shallower than 10 km below the seafloor, indicating that the megathrust can rupture close to the trench.

Key Points:
- Extensional earthquakes in the incoming plate increase to the trench and occur to 35-km depth, consistent with hydration of the mantle
- The heterogeneous distribution of seismicity on the seismogenic zone may reflect the incoming plate roughness and forearc serpentinization
- Earthquakes are identified on the shallow megathrust, showing that thrust faulting extends to depths of less than 10 km and nearly to the trench

Supporting Information:
- Supporting Information S1

Correspondence to:
M. Eimer,
eimer@wustl.edu

Citation:
Eimer, M., Wiens, D. A., Cai, C., Lizarralde, D., & Jasperson, H. (2020). Seismicity of the incoming plate and forearc near the Mariana Trench recorded by ocean bottom seismographs. *Geochemistry, Geophysics, Geosystems*, *21*, e2020GC008953. https://doi.org/10.1029/2020GC008953

Received 3 FEB 2020
Accepted 31 MAR 2020
Accepted article online 6 APR 2020

1. Introduction

Incoming plate bend faulting and shallow megathrust seismogenesis are key components of subduction zone processes. Precise earthquake locations and source mechanisms in the incoming plate and shallow seismogenic zone are essential for understanding these two aspects. Unfortunately, small magnitude earthquakes in the trench region are generally poorly located and studied, since the nearest land-based seismic stations are several hundred kilometers away. Detailed study of seismicity and faulting processes in these

regions require the deployment of ocean bottom seismographs (OBSs). However, only a few near-trench regions have been well studied using OBSs.

The Central Mariana subduction zone subducts some of the oldest oceanic crust on the planet (Müller et al., 1997; Nakanishi et al., 1992). Thus, it has long been identified as an end-member margin to study the subduction zone processes and identified as a type example of subduction zones with backarc spreading and an absence of large megathrust earthquakes (Uyeda & Kanamori, 1979). The old subducting Pacific Plate shows slow upper mantle seismic velocity anomalies, indicating pervasive hydration by water circulation along bending faults, and the slow velocity outer forearc and the presence of forearc serpentine mud volcanoes (Fryer et al., 1995) suggests extensive forearc serpentinization (Cai et al., 2018). The shallow seismogenic zone is of interest with unevenly distributed, low-magnitude events that likely reflect variable conditions along the plate interface (Emry et al., 2011). Here we use records from a yearlong OBS experiment deployed in 2012 near the Central Mariana subduction zone to study the incoming plate and shallow seismogenic zone.

1.1. Bend Faulting and Incoming Plate Hydration

Subduction zones are the main locations where water can be brought back into the deep earth. Hydrous minerals, especially serpentine, make a dominant contribution to this water circulation process (Rüpke et al., 2004; Ulmer & Trommsdorff, 1995; van Keken et al., 2011).

The uppermost mantle is sometimes assumed to be largely anhydrous due to the extraction of water by melting at the mid-ocean ridge (Hirth & Kohlstedt, 1996). However, normal faults resulting from the bending of the incoming plate represent pathways for water to penetrate deep into the subducting slab and hydrate the subducting crust and upper mantle (Naif et al., 2015; Ranero et al., 2003). Normal faulting within the incoming plate seaward of oceanic trenches is observed globally (Craig et al., 2014; Emry & Wiens, 2015), and the bending can produce subhydrostatic or even negative pressure gradients along the faults to promote fluid flow to depth (Faccenda et al., 2009). Serpentinization of the incoming plate mantle has been interpreted in many subduction zones globally, with the amount of hydration dependent on several factors including plate age (Horning et al., 2016), incoming plate fabric (Fujie et al., 2018; Shillington et al., 2015), sedimentation (Contreras-Reyes et al., 2007), and convergence rate (Contreras-Reyes et al., 2011).

The depth of extensional faulting is limited by the neutral plane, which separates the compressional and tensional regimes of the bending plate (Chapple & Forsyth, 1979). Hydration of the mantle is limited to the neutral plane on the basis that water cannot penetrate into the compressional stress regime (Lefeldt & Grevemeyer, 2008). A global average depth to the neutral plane is 30–40 km, though regional studies show variability (Craig et al., 2014; Emry & Wiens, 2015) and there may be a correlation between the neutral plane and the 300–350 °C isotherm (Contreyas-Reyes et al., 2011).

The Pacific Plate subducting at the Mariana Trench has the potential to store a large amount of water in the form of serpentine minerals, since its age is greater than 150 Ma (Nakanishi et al., 1992). The brittle-ductile transition should occur deeper in older plates (Watts, 2001), and the 600 °C isotherm approximating the antigorite stability field occurs at >50-km depth (McKenzie et al., 2005). Surface wave tomography indicates hydration to at least 24 km below the Moho (30 km below the seafloor) based on shear wave velocity reduction (Cai et al., 2018). Geodynamic models matching the bathymetry of the bending plate suggest a 25 km deep neutral plane (relative to seafloor), but are subject to large uncertainties (Emry et al., 2014; Zhou & Lin, 2018). A waveform inversion study of a small number of teleseismic normal faulting earthquakes shows earthquake centroid depths down to 17 km below the seafloor (Emry et al., 2014).

In this study, we use seismograms from an OBS array deployed across the Mariana trench to precisely determine smaller magnitude earthquake source parameters and study faulting on the incoming plate associated with plate bending. Earthquake locations and depths determined by OBS recording are much more accurate than those derived from teleseismic recordings, and local seismicity may be more indicative of the average stress state of the plate (Lefeldt et al., 2012). The depths and focal mechanisms of incoming plate earthquakes provide constraints on the depth extent of normal faulting, and the lateral extent places constraints on the spatial distribution of faulting, which varies between different models (e.g., Emry et al., 2014; Zhou & Lin, 2018).

1.2. The Seismogenic Zone

The seismogenic characteristics of subduction zone megathrust faults vary widely, with some rupturing in large megathrust earthquakes and others showing no great ($M_w > 8$) earthquakes for the duration of recorded history. It has been proposed that the size of earthquakes along the megathrust may be limited or reduced by the influence of subducting topography (Lallemand et al., 2018; Wang & Bilek, 2014), limited sedimentation (Brizzi et al., 2018; Li et al., 2018; Seno, 2017), serpentinization of the mantle wedge (Hirauchi et al., 2010; Reynard, 2013), and/or extensional stress across the forearc (Heuret et al., 2011).

Subducted topography has been shown to correlate with areas of weak coupling along the megathrust (Bassett & Watts, 2015; Lallemand et al., 2018). Although some subducting seamounts have been tied to earthquake generation by locally increasing coupling (Bilek et al., 2003; Yang et al., 2012), subducting topography likely deforms the overriding plate, creating a fracture network that may promote small earthquakes and aseismic creep (Collot et al., 2017; Wang & Bilek, 2011) and reducing coupling through serpentinization of the overriding plate (Singh et al., 2011). Large megathrust earthquakes are unlikely to occur under these conditions, with small asperities rupturing along areas of stable sliding and preventing large asperities from locking and accumulating strain (Emry et al., 2011; Wang & Bilek, 2014).

The Central Mariana subduction zone is considered an aseismic end-member (Uyeda & Kanamori, 1979), with no historical record of megathrust earthquakes greater than M_s 7.4 (Emry et al., 2011). The seismicity along the Mariana megathrust fault is characterized by a heterogeneous distribution, which has been attributed to subducting topography and/or partial serpentinization of the forearc (Emry et al., 2011). There is strong evidence for significant mantle wedge serpentinization, on the basis of active serpentine seamounts on the outer forearc (Fryer, 1996) and seismic imaging of the mantle wedge (Barklage et al., 2015; Cai et al., 2018; Pyle et al., 2010; Tibi et al., 2008), though the distribution may be heterogeneous. These characteristics make it an ideal location to investigate megathrust microseismicity and slip properties that may help explain the absence of larger events.

One of the possible reasons for the lack of large megathrust earthquakes in the Mariana Trench is a proposed narrow zone of thrust faulting (e.g., Hyndman et al., 1997). However, Emry et al. (2011) show that megathrust faulting extends between 20- to 60-km depth and through a width of about 100 km. This is not an unusually narrow width, as the width of the seismogenic zone ranges from 50 to 200 km globally (Herrendörfer et al., 2015). Emry et al. (2011) did find a nearly complete absence of thrust zone earthquakes at depths shallower than 20 km and within 60 km of the trench. Many previous studies have noted similar aseismic regions near the trench, which led to a widespread assumption that the near-trench region was aseismic and deformed by creep (Byrne et al., 1988; Pacheco et al., 1993). However, observations of large slip to the trench during the 2011 Tohoku earthquake (Fujiwara et al., 2011; Lay et al., 2011; Kodaira et al., 2012) and the locations of smaller earthquakes near the trench at several locations (Todd et al., 2018) provide counterexamples. Thus, the processes controlling seismic slip along the megathrust at shallow depths near the trench are poorly understood.

In many subduction zones, the updip limit of seismicity appears to correlate with the 100–150 °C isotherm (Oleskevich et al., 1999; Spinelli & Saffer, 2004), leading to the thought that it is controlled by a change in frictional properties by smectite to illite clay transformation (Hyndman et al., 1997; Vrolijk, 1990). However, laboratory experiments found that illite shale is velocity-strengthening/stable (Saffer & Marone, 2003), but the fluid release during the reaction has also been considered (Lauer et al., 2017; Spinelli & Saffer, 2004). In this case, earthquakes occur downdip of peak fluid release, due to lithification and increased effective stress by reduction in fluid pressure (Heise et al., 2017; Lauer et al., 2017; Saffer, 2017). Updip of the ~150 °C isotherm, pore fluid overpressure prevents seismic slip and instead promotes creep and slow slip events (Ranero et al., 2008; Saffer & Tobin, 2011; Vannucchi et al., 2012). Seismic and magnetotelluric imaging confirm that areas of high water content along the decollement are inversely correlated with seismicity (Bangs et al., 2015; Saffer, 2017).

In this study, we use data collected by an ocean bottom seismic deployment centered around the Mariana Trench to precisely locate and study earthquakes near the trench. This geometry provides better coverage of the outer forearc compared with previous studies in this region and allows better characterization of

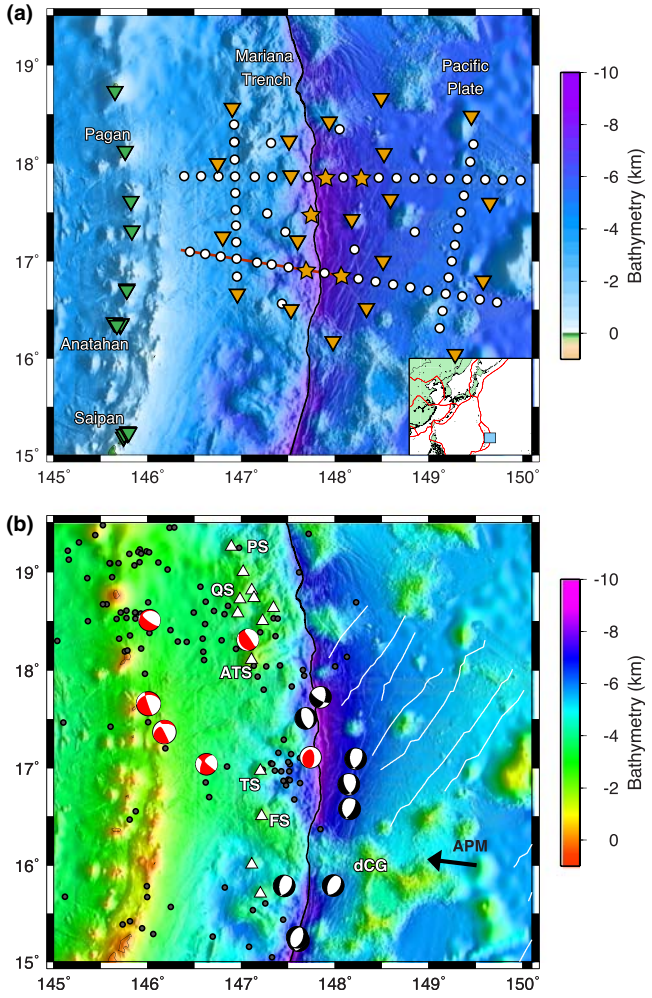

Figure 1. (a) Station distribution for the 2012–2013 deployment. Stations are broadband ocean bottom seismographs (orange inverted triangles), island arc stations (green inverted triangles), and tethered hydrophones (orange stars) used for the entire yearlong experiment. White circles are short period stations and tethered hydrophones from the active source component. Red, thick line indicates location of active source profile shown in Figure 10. Inset shows geographical location of the study, with plate boundaries from Bird (2003). (b) Map highlighting bathymetry in the study region, with earthquakes from the ISC catalog (black circles), focal mechanisms from the GCMT catalog (Dziewonski et al., 1981; Ekström et al., 2012) for the time period of the study (red focal plots) and bend-related normal faults from Emry et al. (2014) (black focal plots). The black arrow denotes the direction of apparent plate motion (Kato et al., 2003), and magnetic lineations are marked by the white lines (Nakanishi et al., 1992). Serpentine seamounts as in Fryer (2012) are denoted by white triangles. ATS, Asùt Tesoru Seamount (Big Blue); FS, Fantangisña Seamount (Celestial); PS, Pacman Seamount; QS, Quaker Seamount; TS, Turquoise Seamount. An incoming plate guyot, del Cano Guyot, is labeled dCG.

the shallow seismogenic zone, including the updip limit of seismicity and heterogeneous nature of the shallow megathrust.

2. Data Analysis

2.1. Data Sets

Seismic data for this study were collected by a seismic deployment across the central Mariana Trench between late January 2012 and February 2013 (Figure 1). The passive source component of the experiment consisted of 20 broadband ocean bottom seismometers (OBS) that straddled the trench, 5 hydrophones tethered in the water column near the trench, and 7 temporary broadband stations deployed on islands along the Mariana arc. The OBSs included 10 Scripps Institute of Oceanography (SIO) instruments, 9 of which included Trillium T240 sensors and 1 with a Trillium T40 sensor, and 10 standard Lamont Doherty Earth Observatory (LDEO) OBSs with modified Sercel L4C 3-component sensors. All OBSs also included a differential pressure gauge. All of the OBSs were recovered and returned good data, except one LDEO instrument, which did not return any data, and one SIO instrument, which returned data only from the differential pressure gauge. The horizontal components from the broadband OBSs were oriented using surface waves from teleseismic earthquakes (Scholz et al., 2017). The tethered hydrophones used LDEO data loggers and were designed to float in the water column ~5 km below sea level. Tethered instruments were required because the instruments were not rated past 6-km depth, whereas the trench reaches 8.6 km below sea level in the study area. Nine island stations from the USGS Northern Mariana Islands Seismograph Network on the islands of Saipan, Anatahan, and Sarigan were also used.

The active source component consisted of an additional 44 short period OBSs and 15 tethered hydrophones that were deployed for about a month at the beginning of the experiment (Figure 1). These instruments were also used to determine *P* and *S* wave arrival times for earthquakes occurring between 1 February to 10 March 2012.

2.2. Earthquake Location

We used a short-term average to long-term average amplitude ratio method (STA/LTA) implemented in the Antelope software package (BRTT Inc, Pavlis et al., 2004) to detect and associate arrivals for potential events occurring within the volume enclosed by 146-150°E, 16-19°N, and 0- to 150-km depth. Arrival time picks were then manually adjusted, added, and used to locate the earthquakes with a Gauss-Newton method using the program dbgenloc (Pavlis et al., 2004). Local magnitudes were also calculated in Antelope, with the median value taken over at least five of the incoming plate OBS and land stations. The LDEO OBS, generally located in the forearc, were not included in the magnitude calculation as the waveforms were clipped for larger events. The calculated local magnitudes are consistent with teleseismic mb values listed for the larger events in the International Seismological Centre online bulletin (Di Giacomo & Storchak, 2016).

The events are then relocated using a probabilistic nonlinear earthquake location method that can utilize a 3D velocity model (NonLinLoc, Lomax et al., 2000). Travel times within the velocity model are calculated using an Eikonal finite-difference scheme (Podvin & Lecomte, 1991). The parameters of the earthquake location problem (latitude, longitude, depth, and time) are described as probability density functions (Tarantola, 1987; Tarantola & Valette, 1982) and determined by nonlinear sampling of the model space.

Each sampled point in the model space is given a probability value based on how predicted travel times compare with the observed travel times. The maximum likelihood hypocenter is determined by finding the point with minimum misfit within the probability density function. Uncertainties are estimated as ellipsoids by calculating the covariance matrix from gridded values of the nonlinear probability density function. The 95% confidence intervals are taken from the covariance matrix. The average semimajor axis of the 95% confidence ellipses is 4.3 km, though it is of consideration that earthquake depths can be harder to constrain at shallower depths (crust and upper mantle) for the array geometry.

An a priori 3D velocity model was constructed to better constrain the locations of earthquakes. The velocity model includes a water layer, derived from bathymetry data interpolated at 1-km intervals (Gardner, 2010). The crustal structure is interpreted from *P* wave velocity models obtained from active source refraction profiles (Calvert et al., 2008; Eimer et al., 2017; Feng, 2016; Takahashi et al., 2008), and the mantle velocity is taken from *S* wave velocity models determined from surface wave tomography (Cai et al., 2018). The model was also modified to remove artifacts due to the parameterization of the surface wave tomography model by smoothing the upper 10 km of the mantle where the tomography can be somewhat unstable right at the Moho. Several models were tested with perturbations in Vp/Vs ratio, % radial anisotropy, and crustal velocity before settling on a model that minimized the root mean square (RMS) residuals for *P* and *S* arrivals of the events. Rather than using a constant Vp/Vs ratio, a linear relationship between Vp and Vs ($Vp = 1.36\ Vs + 1.90$) based on experimental results (Christensen, 2004; Ji et al., 2013; Salisbury & Christensen, 1978) was implemented to determine the *S* velocity for the crust and *P* velocity for the mantle. This equation approximates the change in Vp/Vs ratios due to composition and is roughly consistent with regional models for Vp/Vs ratios from *P* and *S* wave tomography (Barklage et al., 2015) and expected ratios for an oceanic plate (Hyndman, 1979; Kandilarov et al., 2015). The mantle shear velocities from the surface wave tomography model were corrected for radial anisotropy by applying a 1% increase to the observed Sv velocities to obtain the Voigt average *S* velocity, assuming 3% radial anisotropy as is typically found for the uppermost mantle (Montagner, 2007). Changing the velocity model caused some hypocenters to shift more than the calculated 95% confidence intervals, since the confidence intervals assume the a priori velocity model and do not include the dependence on the input velocity model. However, the events shifted less than 5 km for more than 99% of the events for the suite of plausible velocity models tested. An example is shown in Supporting Information, Figure S1, which plots a subset of earthquakes (July–December 2012) on the incoming plate, with locations used in the final model (blue) compared with a model with a different Vp/Vs ratio ($Vp = 1.37\ Vs + 2.02$) (orange). The 95% confidence ellipsoids are plotted, with most earthquakes shifting within the bounds of the error ellipsoids due to the change in velocity model used.

To further understand the earthquake distribution, localized subsets of events were relocated using a double difference relative location method (HypoDD, Waldhauser & Ellsworth, 2000; Waldhauser, 2001). This method reduces the scatter in earthquake locations due to velocity variations by assuming that the ray paths for two adjacent earthquakes are similar to a given station, and thus, the travel time difference between the event pair is due to their spatial offset and not velocity structure along the ray path. A weighted least squares inversion is used to minimize residuals between observed and theoretical travel time differences for pairs of earthquakes at each station. The picked absolute arrival times for *P* and *S* arrivals were used across all available stations, and differential *P* wave arrival times from waveform cross correlation were added when waveforms were similar. To satisfy the condition that earthquake separation is less than event-station distance and scale length of velocity heterogeneity (Waldhauser & Ellsworth, 2000), three clusters were defined and event pairs were required to be within 10 km of each other for absolute arrival times and within 5 km for differential travel times. An additional cluster, which included 348 earthquakes around Asùt Tesoru seamount (informally known as Big Blue Seamount and the largest identified mud volcano in the forearc; Oakley et al., 2007), used absolute travel times with event pair separation of 15 km. To avoid the influence of poorly located earthquakes, only earthquakes with an RMS travel time residual of less than 1 s were included. To best approximate the velocity structure, each cluster used a different local 1D velocity structure based on the 3D velocity model described above.

2.3. Focal Mechanism Determination

Focal mechanisms and seismic moments were determined for the larger events in the catalog using regional waveform inversion. Records of larger events from OBSs located in the forearc were clipped, so we used

OBSs on the incoming plate and the land stations for regional waveform inversion. A nonlinear low-frequency signal on the OBS records affected some of the earthquakes, limiting the number of events that could be studied. Greens functions were calculated using wavenumber integration (Herrmann, 2013). The source time function was estimated as a 1-s parabolic pulse, sufficient for the M_w 4–5 events being studied. Because the wavenumber integration method requires a 1D velocity structure, one of two 1D velocity profiles were used depending on where the station was located (Table S1). A velocity model approximating the incoming plate and including a 5.6-km water layer was used for the OBS, which were all on the incoming plate, and a model approximating the forearc and including a 2-km water layer was used for island arc stations. Three percent radial anisotropy was included in the mantle.

The data were filtered to 0.03–0.06 Hz to minimize the effect of local structure and to minimize long period noise on the horizontal components, and downsampled to 1 Hz. The seismograms were rotated to the great circle path and cut to time windows extending from prior to the origin time until after the surface wave arrival. An amplitude correction was also applied to the OBS records, because of some uncertainty in the nominal OBS gain values. The station amplitude corrections were determined from surface wave amplitudes using a two-plane wave tomography method and a data set of 380 earthquakes (Cai, 2018; Yang & Forsyth, 2006). All vertical, radial, and transverse components with a clear earthquake signal were included in the inversion. Focal mechanisms were solved for using a grid search to find the solution which maximizes fit between the synthetics and data (Herrmann, 2013).

Before determining source parameters for smaller events with no prior source information, we first validated the regional waveform inversion method by determining source parameters for two events during the deployment that have centroid moment tensor (Global Centroid Moment Tensor [GCMT]) solutions (Dziewonski et al., 1981; Ekström et al., 2012). Comparison of the double-couple source mechanisms listed in the GCMT catalog with those determined in this study indicates our procedure, and 1D structure approximation produces reliable results. The solution and waveform fits for a shallow thrust earthquake are shown in Figure 2, including a comparison with the solution given by the GCMT catalog.

Due to the lower seismicity levels and magnitudes of the earthquakes on the incoming plate, the signal to noise ratios at longer periods were insufficient to determine focal mechanisms using waveform inversion. In order to determine mechanisms for these earthquakes, first motion polarities were used instead. Since first motion focal mechanisms tend to be less reliable than those determined by waveform inversion, we selected the largest incoming plate events with good azimuthal coverage to ensure dependable results. Only earthquakes with at least 10 clear *P* polarities were considered, with *SH* polarities included when possible. *SV* polarities were not included because of the phase distortion expected for postcritical incidence angles (Snoke, 2003). As the selected earthquakes were all on the interior of the array, azimuthal coverage was acceptable for events that exceeded the minimum required number of polarities. Take-off angles and station azimuths were calculated using the 3D velocity model, and a grid search over strike, dip, and rake angles was used to find acceptable solutions based on the input polarities (Snoke, 2003). Final mechanisms were taken as the average of the acceptable solutions since the suite of possible solutions for each earthquake were of similar strike/dip/rake. Comparison of the first motion polarity results with two of the GCMT earthquake solutions suggests that focal mechanisms determined with this method are reliable (Figure S2).

3. Results

We located 1,692 earthquakes within the study area using the 3D velocity model (Figure 3). Of the focal mechanisms in this study, 12 were determined using regional waveform inversion in the forearc (Table 1), and 5 were determined using first motion polarities in the incoming plate (Table 2). The magnitude of completeness is M_L 3.4 for earthquakes that met the criteria for determining magnitudes. A *b* value of 1.3 is calculated by linear regression between M_L 3.4–5.5 from the frequency-magnitude distribution (Figure S3).

Earthquakes in the incoming plate prior to subduction, 389 in total, are associated with the bending of the plate. While earthquakes occur at distances up to 167 km from the trench, most of the incoming plate seismicity occurs within 70 km of the axis (Figure 4). Earthquake frequency increases continuously towards the trench, with over half the data set located on the inner trench slope within 30 km of the trench axis.

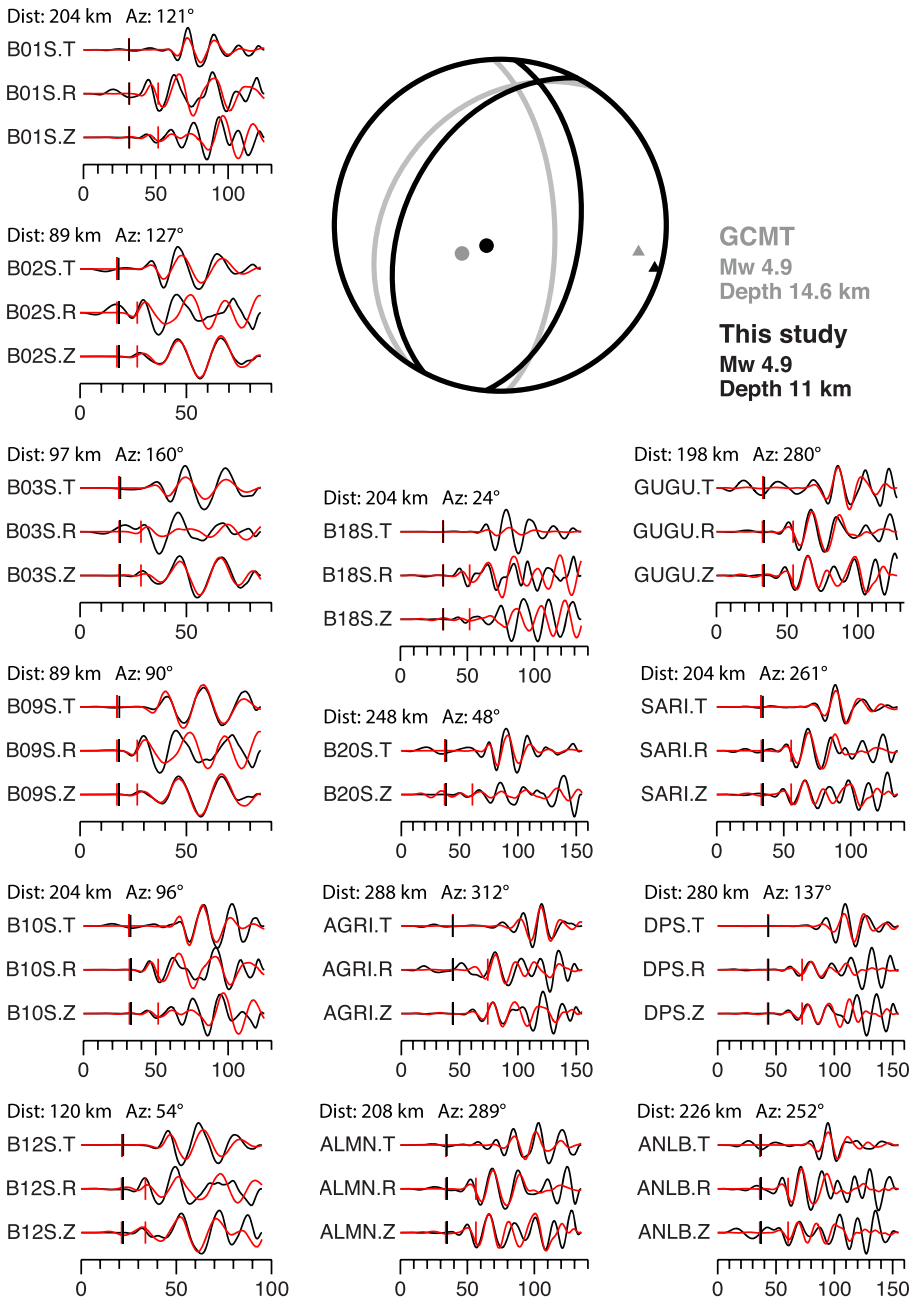

Figure 2. Results from the regional focal mechanism inversion for the 20 May 2012 earthquake at 16.99°N and 147.67°E. All waveforms used in the inversion are shown, with data in black and synthetics in red. The focal mechanism determined by this study is in black, and the GCMT catalog solution is in gray (Dziewonski et al., 1981; Ekström et al., 2012). The *P* axis is marked with a filled triangle and *T* axis with a filled circle for each solution.

Earthquakes on the incoming plate extend down to about 35 km below the seafloor, with a peak at 25-km depth (Figure 5). Although earthquake frequency increases towards the trench, the depth extent appears to be relatively constant with distance from the trench (Figure 6). Focal mechanisms using first motion polarities were determined for five earthquakes on the incoming plate. All five events show extensional focal mechanisms and are located at depths of 23-32 km below the seafloor (Table 2). Most are oriented as expected, with strike subparallel to the trench. One event shows east–west striking nodal planes (25 April 2012), but the fault strike has relatively large uncertainties and a fault plane subparallel to the trench cannot be ruled out.

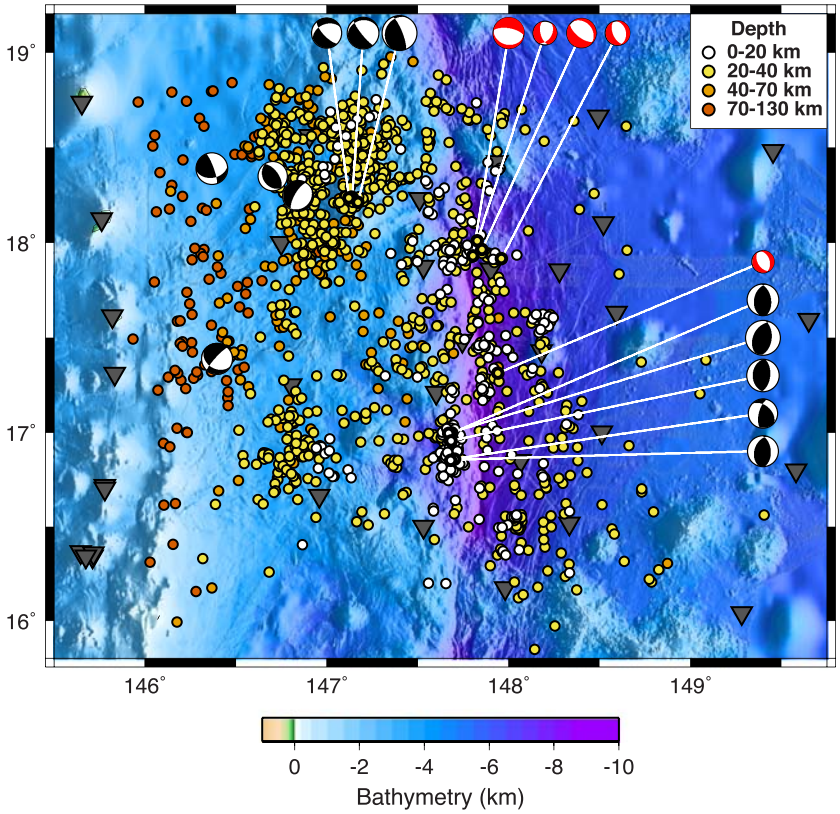

Figure 3. Map of seismicity from this study, color coded by depth below the seafloor. Focal mechanisms determined by regional waveform inversion are in black and by first motion polarities are in red. Sizes are scaled to magnitude. Gray inverted triangles show seismometers used for the yearlong study.

Two major earthquake swarms are identified on the incoming plate (Figure 7). Both sites show recurrent activity through the year, but have a large burst of activity over a 15-day duration for the more northern cluster and 35-day duration for the southern cluster (Figure 7c). Neither cluster shows a traditional mainshock-aftershock sequence, but instead show a continuous distribution of magnitudes between M_L 2.5–3.5. The largest event of both clusters occurs partway through the main swarm of activity. The larger cluster, at 16.5°N, 148°E, is located under a large fault scarp in the bathymetry. The cloud of earthquakes is steeply dipping away from the trench and extends from 21–28 km below the seafloor. There is no migration of events with time, with events occurring throughout the feature for the duration of activity. The smaller cluster, at 17.6°N and 148.2°E, is located just north of a major seamount in a region with several fault scarps, at depths from 17–22 km below the seafloor.

The forearc seismicity consists of several prominent clusters, with the largest between 17.8-18.7°N and 146.7-147.4°E near Asùt Tesoru (Big Blue) seamount, coincident with the largest cluster (Emry et al., 2011) observed using data from the 2003–2004 OBS deployment. A smaller cluster is observed to the south at 17°N and 146.8°E with a relatively quiet corridor between 17.3°N and 17.8°N, confirming the patchy nature of the seismogenic zone in the region. This cluster also maintains a relatively constant rate of seismicity and is a dipping feature, likely delineating the plate interface. The cluster was also observed in the 2003–2004 deployment (Emry et al., 2011), indicating that both clusters are long-term features of the seismogenic zone.

A shallow thrust sequence occurred at 17°N and 147.7°E, within 20 km of the trench. Earthquakes occur throughout the year, but the rate increases after the M_w 4.9 thrust event on 20 May 2012. Focal mechanisms of an earlier and three subsequent events confirm similar mechanisms, with magnitudes M_w 4.5 (19 May), 4.6 (26 May), 4.4 (29 May), and 4.1 (26 September). Double difference relative relocations of all the events in the cluster show earthquakes aligned in the north–south direction and deepening to the north (Figure 8).

Table 1
Focal Mechanism Solutions Determined by Regional Waveform Inversion

Date	Longitude	Latitude	Depth (km)	Strike	Dip	Rake	M_W	M_L
19 May 2012	147.69	17.00	11	350	50	75	4.5	4.1
20 May 2012	147.67	16.99	11	5	50	75	4.9	4.6
26 May 2012	147.68	16.96	11	180	35	85	4.6	4.6
29 May 2012	147.68	16.85	12	355	50	75	4.4	4.2
26 September 2012	147.70	16.86	14	195	65	130	4.1	4.0
11 June 2012	146.40	17.39	54	120	35	−15	4.3	4.8
7 September 2012	146.70	18.35	43	150	30	95	4.1	4.0
23 October 2012	146.84	18.25	38	210	70	−95	4.3	4.3
29 October 2012	146.37	18.39	98	340	80	130	4.4	4.6
16 December 2012	147.17	18.21	33	210	20	140	4.9	4.7
16 December 2012	147.14	18.24	31	260	20	−150	4.4	4.2
19 December 2012	147.12	18.24	30	250	40	−150	4.2	3.8

Note. Depth is given in reference to sea level.

4. Discussion

4.1. Incoming Plate Seismicity

4.1.1. Depth and Temporal Characteristics of Incoming Plate Earthquakes

Near the trench, focal mechanisms and locations determined in this study confirm that normal faulting occurs to depths of 32 km below the seafloor (Table 2), which is deeper than found for a small number of teleseismic earthquake centroids in the same area (Emry et al., 2014). The depths of all incoming plate seismicity, including events without focal mechanisms, extend to at least 35 km below the seafloor (Figure 5). All the earthquakes with focal mechanisms show normal faulting, and the earthquakes seem to represent a single population. If, on the other hand, the earthquake sample crossed the neutral plane and included compressional earthquakes that were too small for focal mechanism determination, an earthquake minimum and a subsequent increase at a deeper depth would be expected. Thus, it is likely that only extensional earthquakes are represented in this study. This depth is consistent with estimates of hydration from seismic tomography, which shows velocity reduction to ~30 km below seafloor (Cai et al., 2018). The correlation of earthquake depths and velocity reductions due to hydration supports the idea that bend faulting is the mechanism through which the crust and mantle are hydrated prior to subduction.

The incoming plate earthquake depths are consistent with a neutral plane about 35 km below seafloor. This is somewhat deeper than predicted by several recent flexural bending models that are constrained by the seafloor elevation profile. Zhou and Lin (2018) predict a maximum depth of normal faulting of 21 km below the seafloor, while Emry et al. (2014) predict a neutral plane at 25 km below the seafloor. However, multichannel seismic images of the outer forearc combined with high-resolution bathymetry at the trench show that the dip angle of the incoming plate abruptly increases at the trench (Oakley et al., 2008). Emry et al. (2014) point out that including the plate interface below the outer forearc landward of the trench, rather than just the incoming plate bathymetry, predicts larger extensional stresses with a neutral plane at 38 km and brittle faulting to 30-km depth. For comparison, focal mechanisms indicate a neutral surface of about 40-km depth for the source region of the 1933 Sanriku earthquake in NE Japan (Obana et al., 2018), and the neutral surface in the incoming plate increased from 20- to 40-km depth after the occurrence of the 2011 Tohoku earthquake (Obana et al., 2012).

Table 2
Focal Mechanism Solutions Determined by First Motion Polarities

Date	Longitude	Latitude	Depth (km)	Strike	Dip	Rake	M_L
5 April 2012	147.94	17.31	32	343	42	−79	2.9
25 April 2012	147.80	17.93	27	280	65	−90	4.4
28 April 2012	147.96	17.92	23	349	34	−80	3.4
16 June 2012	147.86	17.97	30	319	26	−80	4.1
31 July 2012	147.83	18.01	31	31	42	−53	3.3

Note. Depth is given in reference to the seafloor.

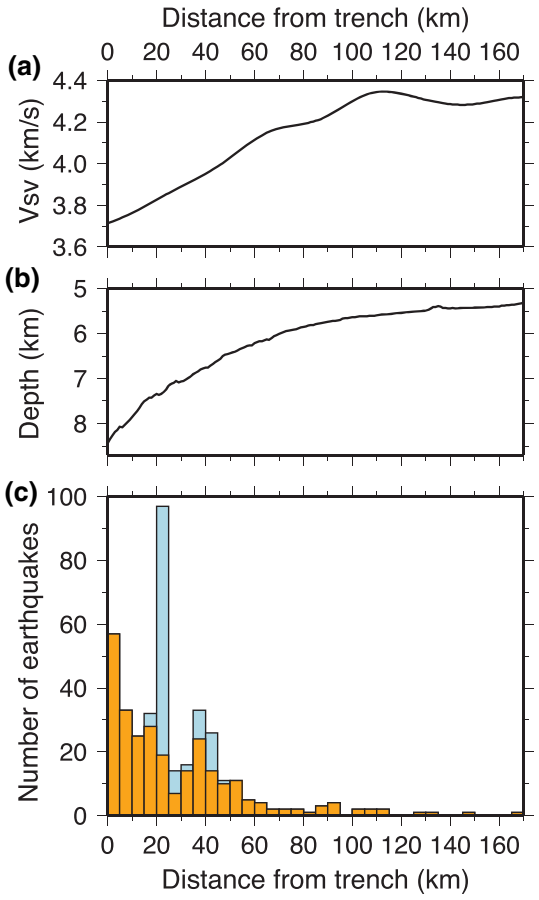

Figure 4. (a) Mantle *S* velocity as a function of distance from the trench at 20-km depth below seafloor, averaged over five profiles along the arc, perpendicular to the trench (Cai et al., 2018). (b) Bathymetry with distance from the trench, averaged over the same five profiles used in panel (a). (c) Histogram of the number of events on the incoming plate as a function of distance from the trench. Blue bars include all earthquakes, and orange bars show results with the two swarms on the incoming plate removed.

A relatively deep neutral plane may be typical for bending of old oceanic plates when the plate is not temporarily loaded by locking on the adjacent megathrust. At strongly coupled subduction zones, changes in the neutral plane allowing for deep, large extensional incoming plate earthquakes have been shown to be temporally linked to large interplate earthquakes (Christensen & Ruff, 1988; Obana et al., 2012). In Central America, local/regional seismicity suggested the neutral plane was shallower (6–9 km below the Moho) than inferred from large extensional earthquakes (15 km below the Moho) (Lefeldt et al., 2009; Lefeldt et al., 2012). The Mariana subduction system is considered poorly coupled (Christensen & Ruff, 1988), and the influence of any interplate earthquakes on the stress conditions in the incoming plate should be reduced. In fact, only one compressional earthquake has been observed teleseismically in southern Mariana, and a lack of compressional earthquakes is consistent with low coupling at Central Mariana.

To further support the influence of bend faulting on plate hydration, the two clusters on the incoming plate exhibit earthquake swarm behavior, which may indicate fluid migration. The swarms are characterized by having no single principal event and a finite time of increased activity (Yamashita, 1998). Swarms observed in both intraplate settings and plate margins are thought to be generated by fluid pressure (Kurz et al., 2004). On the incoming plate off southern Chile, clusters of highly similar earthquakes have been identified and inferred to be caused by seawater infiltration to mantle depths (Tilmann et al., 2008).

Fluids are thought to cause overpressure causing earthquake rupture, which then creates permeability through which the overpressure is diffused, thus arresting further seismic activity. This limits the size of earthquakes and prevents mainshock-aftershock sequences (Yamashita, 1999). With this mechanism, the swarms indicate fluid, in this case oceanic water, along preexisting faults (Tilmann et al., 2008), and is supported by the existence of fault scarps above

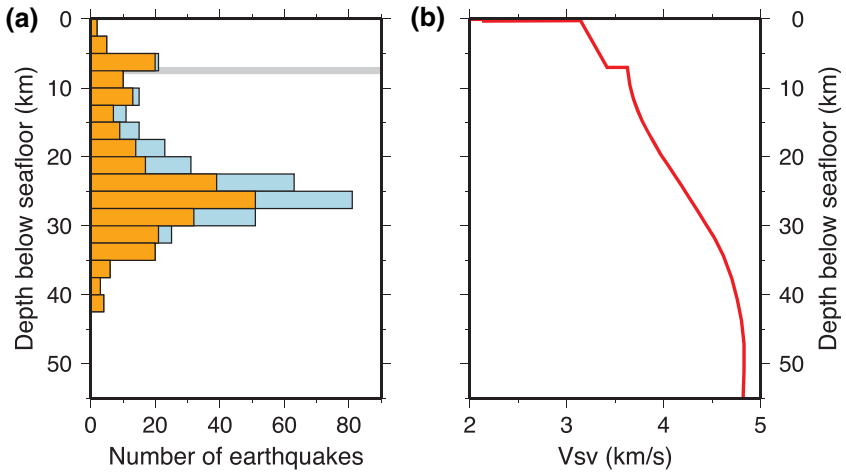

Figure 5. (a) Histogram showing the depth below seafloor for events on the incoming plate. Blue bars include all earthquakes, and orange bars show results with the two swarms on the incoming plate removed. Gray line indicates range of Moho depths. (b) *S* wave velocity profile for the trench high from surface wave tomography (Cai et al., 2018).

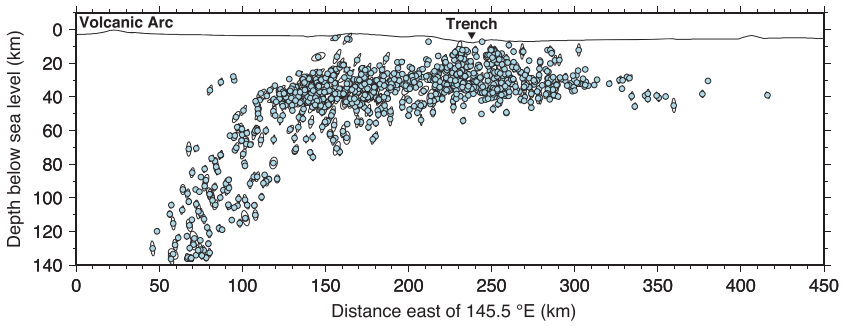

Figure 6. Plot of all earthquakes in the study, as in Figure 3, in cross section. Error ellipses show the 95% confidence regions for the earthquake locations.

both locations of the swarms. Fluid discharge features observed by a human-occupied vehicle (HOV) on the incoming plate in southern Mariana further support fluid cycling along these normal faults (Du et al., 2019).

4.1.2. Onset and Intensity of Faulting

Most of the seismicity is located within 70 km of the trench. The lateral extent of seismicity is consistent with where the seismic velocity starts to rapidly decrease 80 km east of the trench (Cai et al., 2018), indicating the seismicity is a good proxy for where significant hydration occurs. In addition, the seismicity rate increases with decreasing distance to the trench (Figure 4), with the highest seismicity rate per area occurring at the trench. If the rate of seismicity is tied to the surface faults, then increased seismicity should increase the rate of offset growth. This is generally consistent with an increase in offset (Zhou & Lin, 2018), particularly when including the large horst at the trench that is in the process of being subducted along the length of the study region (Oakley et al., 2008). In addition, a larger *S* wave velocity reduction is observed closer to the

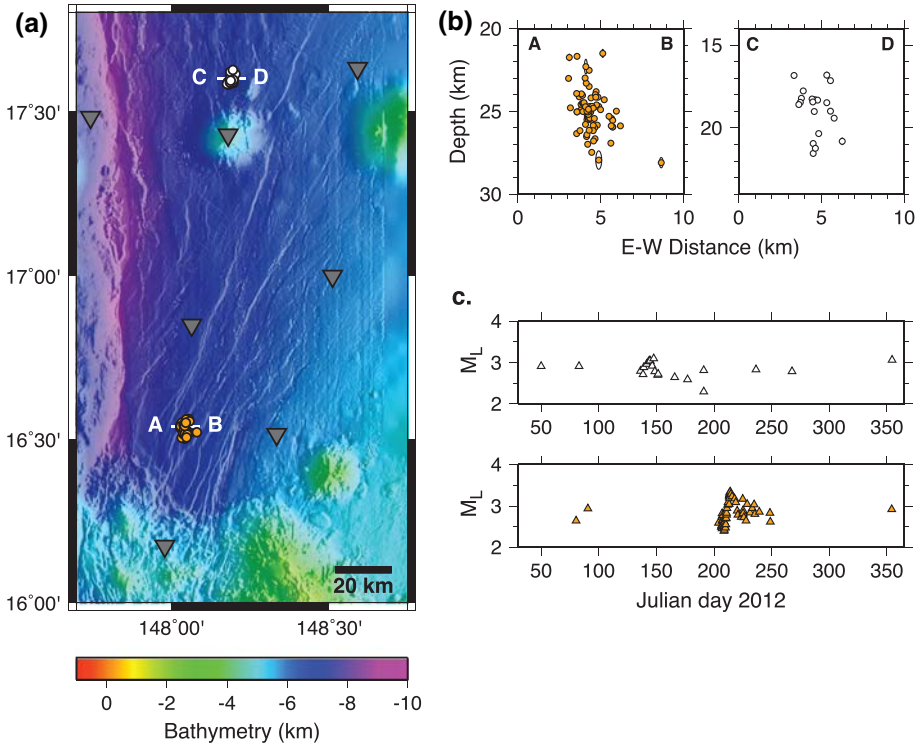

Figure 7. (a) Map view of earthquake swarms on the incoming plate from the double difference location results, color coded by location with the southern cluster events shown by orange circles and northern cluster earthquakes by white circles. (b) Cross sections of swarms, with depth given as depth below seafloor. (c) Local magnitude (M_L) versus time plots.

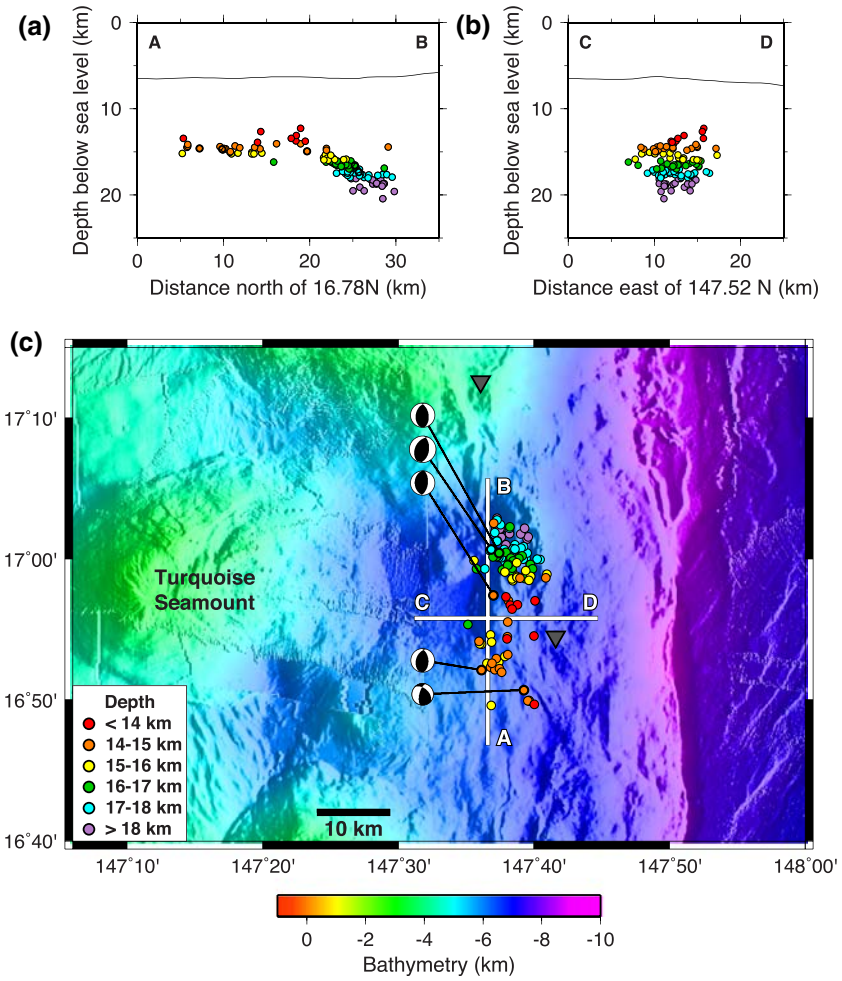

Figure 8. Relative relocation of earthquakes at the shallow thrust sequence, color coded by depth below sea level. North–south (a) and east–west (b) cross sections of the relocated earthquakes, with all earthquakes from map view plotted. (c) Map view of earthquakes and locations of the profiles in panels (a) and (b).

trench (Cai et al., 2018), as would be expected for progressive hydration of the crust and mantle through bend faulting as the faults approach the trench. An interesting conclusion of these results is that stress and deformation in the plate are concentrated at the trench axis, instead of the outer rise as often described in the literature and in geodynamic modeling.

While the seismicity rate drops off east of 70 km from the trench, there are earthquakes occurring farther east, with three events occurring at distances larger than 130 km. Alteration of the incoming plate has been observed out to 140 km in seismic refraction profiles at the Kuril Trench (Fujie et al., 2013) and has been suggested as far out as 100–500 km out on the basis of lower than average crustal velocities in the southwestern and northwestern Pacific (Grevemeyer et al., 2018). The earthquakes observed farthest eastward from the Mariana Trench may indicate the influence of bending and the potential to alter the oceanic plate out to at least 170 km. Alternatively, these earthquakes may represent the background intraplate seismicity in the Pacific Plate.

The lateral extent of significant seismicity, although in approximate agreement with the lateral extent of fault scarps in the bathymetry, does not match regional variations observed from north to south. The onset of faulting as determined by fault scarps mapped on the seafloor appears to roughly correlate with the 6-km bathymetric contour, which varies from about 95 km from the trench axis at 18°N to roughly 55 km at 16.5°N (Oakley et al., 2008). Bending-related seismicity occurs beyond this in the south to at least 90 km, indicating that brittle deformation occurs farther out than surficial expressions of faulting here. Small earthquakes

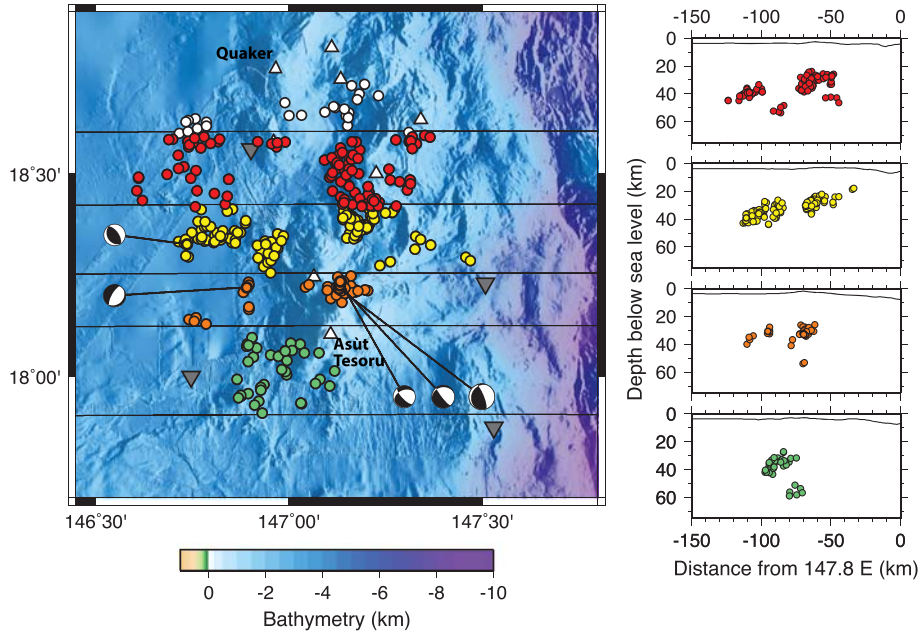

Figure 9. Relative relocations of earthquakes in the northern cluster near Asùt Tesoru (Big Blue) Seamount (labeled). Additional seamounts are denoted by white triangles. The earthquakes included in each cross section are color coded, with the horizontal lines in map view showing the boundaries for each section. Focal mechanisms for five larger earthquakes are also plotted.

likely occur on developing faults that do not yet come to the surface, or are too small to be visible in the bathymetry. In contrast, seismicity at 18°N is largely constrained to within 30 km of the trench, while faulting in the bathymetry is observed to 95 km. This may indicate an aseismic component in fault building, or that the yearlong deployment did not capture the full extent of incoming plate seismicity.

The seismicity rate is noticeably greater on the incoming plate south of ~17.7°N, especially at distances less than 20 km from the trench axis. This correlates with a visible change in fault scarp direction in bathymetry, with Oakley et al. (2008) identifying a change at 17.6°N with new faults formed due to bending to the north, and coexistence of new and reactivated abyssal hill fabric to the south. Reactivation of abyssal hill faults occurs when the plate fabric strikes <25°–30° from the trench axis (Billen et al., 2007; Masson, 1991). In Alaska, alignment of incoming plate fabric at the Shumagin gap results in bend faulting and hydration compared with the Semidi segment where the plate fabric is oblique (Shillington et al., 2015). However, in Japan, more plate hydration is observed at the Japan Trench with oblique plate fabric, compared with the Kuril Trench with subparallel fabric. The difference is attributed to larger fault offsets at the Japan Trench compared with the reactivated faults at the Kuril Trench (Fujie et al., 2018). Given the ambiguous relationship between incoming plate parameters and degree of hydration, it is unclear if the alignment in fabric would promote more hydration in the south where the seismicity rate is greater.

4.2. Forearc Seismicity

4.2.1. Heterogeneous Pattern of Seismicity

The forearc seismicity in this study is marked by a heterogeneous distribution of moderate and low-magnitude events ($M_w < 5$), with clustering in the northern and southern parts of the study region separated by a relatively quiet gap. Relative relocation of the northern cluster near Asùt Tesoru seamount shows structure within the cluster, with small highly seismic regions located on a dipping interface (Figure 9). In cross section, the earthquakes appear to delineate the seismogenic zone from 20–45 km below sea level, although there are deeper events that occur within the plate and may be the updip limit of the lower plane of the double seismic zone (Shiobara et al., 2010), as also observed in Emry et al. (2011).

The subcluster just north of Asùt Tesoru at approximately 18°10′N and 147°10′E includes three events with focal mechanisms, the largest a M_w 4.9 on 16 December 2012, followed by a M_w 4.4 19.3 h later and a M_w 4.2 3 days later (Figure 9). The rate of seismicity also increases following the 16 December event, suggesting an

aftershock sequence. Directly to the west at 18°15′N and 146°50′E, the focal mechanism of the 23 October 2012 event is extensional, suggesting that it occurs in either the subducting slab or overriding plate. With the exception of the aftershock sequence, the earthquakes do not temporally cluster and do not exhibit swarm-like behavior as described in Holtkamp and Brudzinski (2011). The clusters are persistent features, having been observed in previous seismic studies from ocean bottom seismic arrays located closer to the island arc (Emry et al., 2011; Shiobara et al., 2010). Larger GCMT catalog events tend to occur around the edges of the cluster (Emry et al., 2011).

Given the rough topography currently subducting in this region, topography on the downgoing plate may be responsible for the clusters. A negative correlation between large earthquakes and rough incoming plate bathymetry has been observed (Bassett & Watts, 2015; Kelleher & McCann, 1976), and geodetic observations suggest that rough bathymetry promotes creeping as the mode of subduction (Wang & Bilek, 2014). The incoming Pacific Plate at the Mariana Trench is marked by several seamounts, particularly to the north and in the south of the study region where there are loose chains of guyots. The irregularity of the trench depth and axis suggests that topographic features have been subducted (Fryer & Smoot, 1985; Oakley et al., 2008) and active seamount subduction is occurring with the subduction of Dutton Ridge to the north and del Cano Guyot to the south. The irregular nature of the seamount distribution prevents identification of recently subducted seamount locations on the downgoing plate. However, past seamount subduction may have developed a fracture network downdip that would promote small earthquakes and creep while inhibiting large events (Wang & Bilek, 2014).

Globally, subducted seamounts have led to eroded frontal prisms and local seafloor uplift (Kopp, 2013). The Mariana margin does not exhibit significant forearc deformation from seamount subduction, possibly due to a weak serpentinized mantle wedge and/or progressive fracturing of the incoming plate (Oakley et al., 2008), making it difficult to identify subducted features. Active seamount subduction can be observed to the north in the region east of Asùt Tesoru (~18.5°N), causing a shallower trench and displaced overriding plate toe (Oakley et al., 2008). Bassett and Watts (2015) used residual bathymetry to identify the subducting anomaly continuing into the forearc, suggesting that the seamount had subducted relatively intact to depth <20 km. The largest earthquake cluster is observed west of this feature, but seamount subduction to such downdip extent cannot be assumed given the irregular distribution of seamounts on the incoming plate. That being said, the seismicity is consistent with seamount subduction, with low-magnitude events being observed as a long-term feature in this location (Collot et al., 2017).

The coincident location of seismicity clusters and forearc serpentine seamounts may further indicate the influence of subducted topography. The large cluster in the north is below and downdip of Asùt Tesoru, Quaker, and several other smaller seamounts, and the southern cluster is downdip of Turquoise and Fantangisña Seamounts. These seamounts are thought to be long-lived features, with Fantangisña estimated to be at least 10.77 Ma (Menapace et al., 2019). These serpentine seamounts are built over deep-seated extensional faults that formed due to slab rollback and increased curvature of the arc (Fryer et al., 2006; Menapace et al., 2019). Vertical tectonism caused by the subduction of plate seamounts likely furthers the development of these faults that penetrate the forearc to allow serpentinite muds to travel to the seafloor (Fryer et al., 2000; Oakley et al., 2007; Stern & Smoot, 1998). The fact that both clusters can be associated to serpentine seamounts in the study region may lend to the idea that deformation of the overriding plate leads to conditions unable to support large megathrust earthquakes but preferentially rupture in small magnitude events.

The lack of seismicity between the two clusters could indicate two end-member scenarios: an aseismically creeping or a locked region. In Alaska, the Shumigan section of the megathrust, known to be creeping from geodetic measurements, shows a strong cluster of seismicity, whereas sections that are locked are relatively aseismic (Shillington et al., 2015). This may suggest that the aseismic sections of the Mariana trench are locked and have strong earthquake potential. However, global studies have attributed decoupled subduction zones to several parameters including extensional upper plate stress (Heuret et al., 2011; Heuret et al., 2012; Scholz & Campos, 2012), thin and heterogeneous trench fill (Brizzi et al., 2018; Heuret et al., 2011; Li et al., 2018; Seno, 2017), a serpentinized shallow mantle wedge (Reynard, 2013), and/or rough incoming plate topography (Bassett & Watts, 2015; Kelleher & McCann, 1976; Wang & Bilek, 2011). All of these parameters are favorable in Mariana, and it is possible that the seismic gap observed in the center of the study

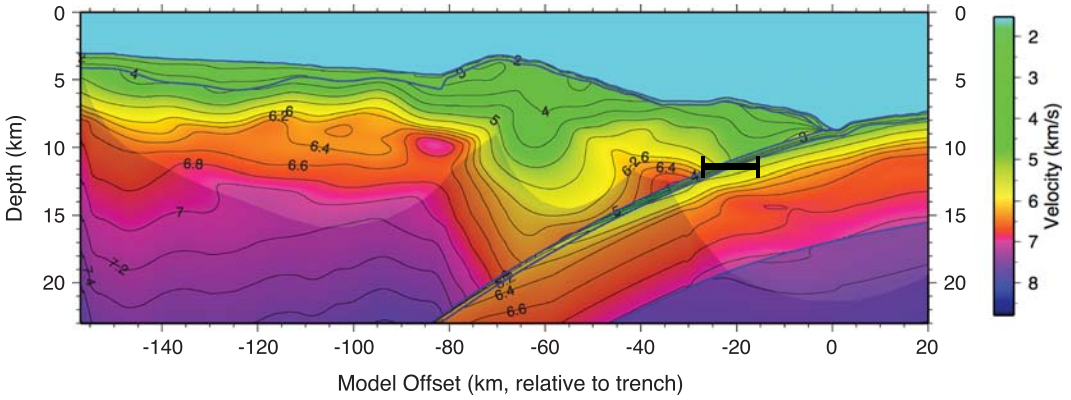

Figure 10. *P* velocity profile inverted from wide-angle refraction data (Eimer, 2020) along a profile that is colocated with the shallow thrust sequence (Figure 1a). Dark shaded areas indicate model space that is not sampled by data in the tomographic inversion. The black bar shows the lateral position and extent of the shallow thrust sequence, which is assumed to lie along the megathrust due to the thrust faulting mechanisms and the waveform inversion depths. The shallow thrust sequence coincides with an increase in seismic velocity at the base of the forearc, suggesting structural control on the event locations.

area is aseismically creeping. However, without geodetic measurements, it is difficult to confirm that the seismogenic zone, especially in the quiescent region, is aseismically slipping rather than locked.

4.2.2. Shallow Thrust Sequence and Updip Limit of Seismicity

This study observed a shallow thrust sequence at 16.9°N and 147.7°E, located at just 20 km west of the trench (Figure 8). The plate interface at this location is expected to be about 5 km below the seafloor (11 km below sea level) from multichannel seismic (MCS) reflection profiles (Oakley et al., 2008), which is consistent with depths from waveform inversion. The relative relocation results, however, locate the earthquakes at 6–14 km below the seafloor, or a few kilometers deeper than the expected slab surface. Choosing different starting locations for the earthquakes and utilizing different velocity structures in the relative relocation suggest that the internal structure of the cluster is robust, and relative location uncertainties (<1 km in depth) are much smaller than the variation in depth between the north and south end of the cluster. However, the absolute depth is dependent on the starting location and velocity structure. Given that all five events with focal mechanisms show thrust faulting, as expected for earthquakes along the megathrust, and the uncertainty in absolute location, the earthquakes are assumed to be on the plate interface.

Relative relocation shows that the events are aligned north–south, parallel to the fault strike from the focal mechanisms, with the shallowest earthquakes in the center and events deepening to the north (Figure 8). Thrust focal mechanisms are consistent with the sequence occurring along the seismogenic zone, so the variation in event depth reflects along-strike variation in the megathrust interface. The slab surface interpreted from previous reflection profiles shows that the plate is not a planar surface, but has along-strike undulations; the plate is shallowest at del Cano Guyot, south of the shallow thrust sequence at 16°N, due to the influence of the subducting seamount structure (Oakley et al., 2008). While the plate surface under this thrust sequence was not surveyed in the Oakley study, a general deepening of earthquakes north of the thrust sequence supports the plate deepening to the north.

Previously, the seismogenic zone was established to be at least 100 km wide, with the updip and downdip limits at 20 and 60 km, respectively (Emry et al., 2011). The thrust sequence in this study shows that the seismogenic zone is active shallower than the previous estimate, increasing the width of the seismogenic zone. While the previous limit coincided with the 150 °C isotherm that has been proposed to be the control on the updip limit (Oleskevich et al., 1999; Spinelli & Saffer, 2004), the new results show that the megathrust can rupture at colder temperatures in this location. This increases the total width of the seismically active thrust fault to 140 km by expanding the updip limit from Emry et al. (2011), further reinforcing the conclusion that the lack of large earthquakes in the Mariana subduction zone is not due to a narrow seismogenic zone (Emry et al., 2011).

Previous studies estimating the temperature along the Mariana megathrust fault, based on pore water chemistry from the serpentine mud volcanoes, suggest that the 80 °C isotherm occurs at 15-km depth, with temperatures reaching 150 °C at slab depths of 17–24 km (Hulme et al., 2010). If seismogenesis is temperature

controlled, diagenetic and low-grade metamorphic reactions occurring at temperatures as low as ~60 °C have the potential to create conditions that support stick-slip behavior (Marcaillou et al., 2008; Moore & Saffer, 2001; Saffer & Tobin, 2011). However, recent estimates of temperature based on oxygen isotope thermometry suggest temperatures as high as 180 °C under Yinazao Seamount at 13-km depth to slab (Debret et al., 2019), which is consistent with the hypothesis that the updip limit is controlled by the 100–150 °C isotherm.

Alternatively, the shallow Mariana subduction zone may be unable to maintain high overpressure, instead dewatering through the forearc. The topography above the thrust sequence is of interest, with a local high above the shallowest part of the sequence (Figure 8). This may indicate deformation of the overriding plate caused by increased coupling along the megathrust, perhaps caused by the uneven plate surface and subducted topography. Structure on the plate may allow for locking of the plate locally by enhanced drainage and higher effective stress (Bilek et al., 2003; Saffer, 2017; Tréhu et al., 2012). A similarly shallow thrust sequence observed off the coast of Costa Rica at the Middle America Trench may be the result of, in part, dewatering due to subduction of the hotter Cocos Ridge (Arroyo et al., 2014).

Structural control on the location of the shallowest thrust events is also indicated by seismic structure obtained from a coincident active source survey. We compare the location of the shallow thrust sequence with a colocated 2D *P* wave velocity profile collected during the active source component of the 2012–2013 seismic experiment (Eimer, 2020). Despite significant depth uncertainties in the relocations, we assume that the shallow thrust earthquakes are located along the megathrust, as indicated by their shallow thrust focal mechanisms and the shallower depths indicated by the waveform inversion. The lateral location of the seismicity cluster correlates with an increase in seismic velocity in the forearc above the plate interface (Figure 10). The increase in seismic velocity may provide additional evidence for dewatering and/or existence of more competent material that is allowing for locking of the interface at shallow depth.

5. Conclusions

1. The incoming plate seismicity indicates a neutral plane of about 35-km depth, which may be the controlling factor for mantle hydration of the incoming plate. The distribution of seismicity is consistent with the depth and lateral extent of the velocity reduction observed from seismic tomography (Cai et al., 2018), supporting bend faulting as the mechanism by which the plate is hydrated.
2. Although earthquakes are observed out to 167 km from the trench, significant seismicity begins about 70 km from the trench and the rate increases continuously towards the trench. This indicates that the largest bending deformation occurs at the trench axis, rather than along the outer rise as sometimes found in modeling studies.
3. The heterogeneous distribution of seismicity may reflect the incoming plate roughness and related forearc serpentinization. The rough incoming plate may also encourage the rupture of small earthquakes and discourage large megathrust earthquakes.
4. The shallow thrust sequence suggests that the updip limit of seismicity is less than 10 km depth and within 20 km of the trench, and may be tied to dewatering, diagenesis, and/or low-grade metamorphism.

Acknowledgments
We thank the captains, crew, and science teams on the R/V Thompson, Langseth and Melville, Dr. Patrick Shore for providing data management and technical support, and Ivan Komarov and Zhengyang Zhou for assistance with data analysis. We thank Ingo Grevemeyer and an anonymous reviewer for their comments to improve the manuscript. Instrumentation and technical support was provided by the PASSCAL program of the Incorporated Research Institutions in Seismology (IRIS) and the Woods Hole, Lamont-Doherty, and Scripps facilities of the Ocean Bottom Seismograph Instrumentation Pool (OBSIP). Funding was provided by the MARGINS/GeoPRISMS program through NSF grant OCE-0841074 (D.A. W.) and the Spencer T. and Ann W. Olin Fellowship program at Washington University in Saint Louis. Raw seismic data used in this study are available through the Data Management Center of the Incorporated Research Institutions for Seismology (http://www.iris.edu/dms/nodes/dmc) under network IDs XF and MI.

References

Arroyo, I. G., Grevemeyer, I., Ranero, C. R., & von Huene, R. (2014). Interplate seismicity at the CRISP drilling site: The 2002 Mw 6.4 Osa Earthquake at the southeastern end of the Middle America Trench. *Geochemistry, Geophysics, Geosystems*, *15*, 3035–3050. https://doi.org/10.1002/2014GC005359

Bangs, N. L., McIntosh, K. D., Silver, E. A., Kluesner, J. W., & Ranero, C. R. (2015). Fluid accumulation along the Costa Rica subduction thrust and development of the seismogenic zone. *Journal of Geophysical Research: Solid Earth*, *120*(1), 67–86. https://doi.org/10.1002/2014JB011265

Barklage, M., Wiens, D. A., Conder, J. A., Pozgay, S., Shiobara, H., & Sugioka, H. (2015). *P* and *S* velocity tomography of the Mariana subduction system from a combined land-sea seismic deployment. *Geochemistry, Geophysics, Geosystems*, *16*(3), 681–704. https://doi.org/10.1002/2014GC005627

Bassett, D., & Watts, A. B. (2015). Gravity anomalies, crustal structure, and seismicity at subduction zones: 1. Seafloor roughness and subducting relief. *Geochemistry, Geophysics, Geosystems*, *16*(5), 1508–1540. https://doi.org/10.1002/2014GC005684

Bilek, S. L., Schwartz, S. Y., & DeShon, H. R. (2003). Control of seafloor roughness on earthquake rupture behavior. *Geology*, *31*(5), 455–458. https://doi.org/10.1130/0091-7613(2003)031<0455:COSROE>2.0.CO;2

Billen, M., Cowgill, E., & Buer, E. (2007). Determination of fault friction from reactivation of abyssal-hill faults in subduction zones. *Geology*, *35*(9), 819–822. https://doi.org/10.1130/G23847A.1

Bird, P. (2003). An updated digital model of plate boundaries. *Geochemistry, Geophysics, Geosystems*, *4*(3).

Brizzi, S., Sandri, L., Funiciello, F., Corbi, F., Piromallo, C., & Heuret, A. (2018). Multivariate statistical analysis to investigate the subduction zone parameters favoring the occurrence of giant megathrust earthquakes. *Tectonophysics*, *728–729*, 92–103. https://doi.org/10.1016/j.tecto.2018.01.027

Byrne, D. E., Davis, D. M., & Sykes, L. R. (1988). Loci and maximum size of thrust earthquakes and the mechanics of the shallow region of subduction zones. *Tectonics*, *7*(4), 833–857. https://doi.org/10.1029/TC007i004p00833

Cai, C. (2018). *Seismic structure near the Mariana Trench and deep earthquake triggering in the Tonga flat slab (Doctoral dissertation)*. Saint Louis, MO: Washington University in Saint Louis.

Cai, C., Wiens, D. A., Shen, W., & Eimer, M. (2018). Water input into the Mariana subduction zone estimated from ocean-bottom seismic data. *Nature*, *563*, 389–392. https://doi.org/10.1038/s41586-018-0655-4

Calvert, A. J., Klemperer, S. L., Takahashi, N., & Kerr, B. C. (2008). Three-dimensional crustal structure of the Mariana island arc from seismic tomography. *Journal of Geophysical Research*, *113*(B1), 1–24. https://doi.org/10.1029/2007JB004939

Chapple, W. M., & Forsyth, D. W. (1979). Earthquakes and bending of plates at trenches. *Journal of Geophysical Research*, *84*(B12), 6729–6749. https://doi.org/10.1029/JB084iB12p06729

Christensen, D. H., & Ruff, L. J. (1988). Seismic coupling and outer rise earthquakes. *Journal of Geophysical Research*, *93*(B11), 13421–13444.

Christensen, N. I. (2004). Serpentinites, peridotites, and seismology. *International Geology Review*, *46*(9), 795–816. https://doi.org/10.2747/0020-6814.46.9.795

Collot, J.-Y., Sanclemente, E., Nocquet, J.-M., Leprêtre, A., Ribodetti, A., Jarrin, P., et al. (2017). Subducted oceanic relief locks the shallow megathrust in central Ecuador. *Journal of Geophysical Research: Solid Earth*, *122*(5), 3286–3305. https://doi.org/10.1002/2016JB013849

Contreras-Reyes, E., Grevemeyer, I., Flueh, E. R., Scherwath, M., & Heesemann, M. (2007). Alteration of the subducting oceanic lithosphere at the southern central Chile trench-outer rise. *Geochemistry, Geophysics, Geosystems*, *8*(7). https://doi.org/10.1029/2007GC001632

Contreras-Reyes, E., Grevemeyer, I., Watts, A. B., Flueh, E. R., Peirce, C., Moeller, S., & Papenberg, C. (2011). Deep seismic structure of the Tonga subduction zone: Implications for mantle hydration, tectonic erosion, and arc magmatism. *Journal of Geophysical Research: Solid Earth*, *116*(B10). https://doi.org/10.1029/2011JB008434

Craig, T. J., Copley, A., & Jackson, J. (2014). A reassessment of outer-rise seismicity and its implications for the mechanics of oceanic lithosphere. *Geophysical Journal International*, *197*(1), 63–89. https://doi.org/10.1093/gji/ggu013

Debret, B., Albers, E., Walter, B., Price, R., Barnes, J. D., Beunon, H., et al. (2019). Shallow forearc mantle dynamics and geochemistry: New insights from IODP Expedition 366. *Lithos*, *326–327*, 230–245. https://doi.org/10.1016/j.lithos.2018.10.038

Di Giacomo, D., & Storchak, D. A. (2016). A scheme to set preferred magnitudes in the ISC Bulletin. *Journal of Seismology*, *20*(2), 555–567. https://doi.org/10.1007/s10950-015-9543-7

Du, M., Peng, X., Seyfried, W. E., Ta, K., Guo, Z., Chen, S., et al. (2019). Fluid discharge linked to bending of the incoming plate at the Mariana subduction zone. *Geochemical Perspectives Letters*, *11*, 1–5. https://doi.org/10.7185/geochemlet.1916

Dziewonski, A. M., Chou, T.-A., & Woodhouse, J. H. (1981). Determination of earthquake source parameters from waveform data for studies of global and regional seismicity. *Journal of Geophysical Research*, *86*(B4), 2825–2852. https://doi.org/10.1029/JB086iB04p02825

Eimer, M. (2020). *The seismicity and shallow structure of the forearc and incoming plate at the Mariana subduction zone* (Doctoral dissertation). Saint Louis, MO: Washington University in Saint Louis.

Eimer, M., Wiens, D. A., Lizarralde, D., & Cai, C. (2017). P-wave velocity structure across the Mariana Trench and implications for hydration. AGU Fall Meeting Abstracts.

Ekström, G., Nettles, M., & Dziewoński, A. M. (2012). The global CMT project 2004-2010: Centroid-moment tensors for 13,017 earthquakes. *Physics of the Earth and Planetary Interiors*, *200–201*, 1–9. https://doi.org/10.1016/j.pepi.2012.04.002

Emry, E. L., & Wiens, D. A. (2015). Incoming plate faulting in the Northern and Western Pacific and implications for subduction zone water budgets. *Earth and Planetary Science Letters*, *414*, 176–186. https://doi.org/10.1016/j.epsl.2014.12.042

Emry, E. L., Wiens, D. A., & Garcia-Castellanos, D. (2014). Faulting within the Pacific Plate at the Mariana Trench: Implications for plate interface coupling and subduction of hydrous minerals. *Journal of Geophysical Research: Solid Earth*, *119*(4), 3076–3095. https://doi.org/10.1002/2013JB010718

Emry, E. L., Wiens, D. A., Shiobara, H., & Sugioka, H. (2011). Seismogenic characteristics of the Northern Mariana shallow thrust zone from local array data. *Geochemistry, Geophysics, Geosystems*, *12*(12). https://doi.org/10.1029/2011GC003853

Faccenda, M., Gerya, T. V., & Burlini, L. (2009). Deep slab hydration induced by bending-related variations in tectonic pressure. *Nature Geoscience*, *2*(11), 790–793. https://doi.org/10.1038/ngeo656

Feng, H. S.-H. (2016). *Seismic constraints on the processes and consequences of secondary igneous evolution of Pacific oceanic lithosphere* (Doctoral dissertation). Woods Hole, MA: Massachusetts Institute of Technology and Woods Hole Oceanographic Institution.

Fryer, P. (1996). Evolution of the Mariana Convergent Plate Margin System. *Review of Geophysics*, *34*(1), 89–125. https://doi.org/10.1029/95RG03476

Fryer, P. (2012). Serpentinite mud volcanism: Observations, processes, and implications. *Annual Review of Marine Science*, *4*, 345–373. https://doi.org/10.1146/annurev-marine-120710-100922

Fryer, P., Gharib, J., Ross, K., Savov, I., & Mottl, M. J. (2006). Variability in serpentinite mudflow mechanisms and sources: ODP drilling results on Mariana forearc seamounts. *Geochemistry, Geophysics, Geosystems*, *7*(8). https://doi.org/10.1029/2005GC001201

Fryer, P., Lockwood, J. P., Becker, N., Phipps, S., & Todd, C. S. (2000). Significance of serpentine mud volcanism in convergent margins. *Ophiolites and Oceanic Crust: New Insights from Field Studies and the Ocean Drilling Program*, *349*, 35–51. https://doi.org/10.1130/0-8137-2349-3.35

Fryer, P., Mottl, M., Johnson, L., Haggerty, J., Phipps, S., & Maekawa, H. (1995). Serpentine bodies in the forearcs of Western Pacific convergent margins: Origin and associated fluids. In B. Taylor, & J. Natland (Eds.), *Active Margins and Marginal Basins of the Western Pacific*, *Geophysical Monograph Series* (Vol. 88, pp. 259–279). Washington DC: American Geophysical Union. https://doi.org/10.1029/GM088p0259

Fryer, P., & Smoot, N. C. (1985). Processes of seamount subduction in the Mariana and Izu-Bonin trenches. *Marine Geology*, *64*(1–2), 77–90. https://doi.org/10.1016/0025-3227(85)90161-6

Fujie, G., Kodaira, S., Kaiho, Y., Yamamoto, Y., Takahashi, T., Miura, S., & Yamada, T. (2018). Controlling factor of incoming plate hydration at the north-western Pacific margin. *Nature Communications*, *9*(3844). https://doi.org/10.1038/s41467-018-06320-z

Fujie, G., Kodaira, S., Yamashita, M., Sato, T., Takahashi, T., & Takahashi, N. (2013). Systematic changes in the incoming plate structure at the Kuril Trench. *Geophysical Research Letters*, *40*(1), 88–93. https://doi.org/10.1029/2012GL054340

Fujiwara, T., Kodaira, S., No, T., Kaiho, Y., Takahashi, N., & Kaneda, Y. (2011). The 2011 Tohoku-Oki earthquake: Displacement reaching the trench axis. *Science*, *334*(6060), 1240. https://doi.org/10.1126/science.1211554

Gardner, J. V. (2010). *U.S. Law of the Sea cruises to map sections of the Mariana Trench and the eastern and southern insular margins of Guam and the Northern Mariana Islands*. Durham, NH: University of New Hampshire.

Grevemeyer, I., Ranero, C. R., & Ivandic, M. (2018). Structure of oceanic crust and serpentinization at subduction trenches. *Geosphere*, *14*(2), 1–24. https://doi.org/10.1130/GES01537.1

Heise, W., Caldwell, T. G., Bannister, S., Bertrand, E. A., Ogawa, Y., Bennie, S. L., & Ichihara, H. (2017). Mapping subduction interface coupling using magnetotellurics: Hikurangi margin, New Zealand. *Geophysical Research Letters*, *44*(18), 9261–9266. https://doi.org/10.1002/2017GL074641

Herrendörfer, R., van Dinther, Y., Gerya, T., & Dalguer, L. A. (2015). Earthquake supercycle in subduction zones controlled by the width of the seismogenic zone. *Nature Geoscience*, *8*, 471–474. https://doi.org/10.1038/NGEO2427

Herrmann, R. B. (2013). Computer programs in seismology: An evolving tool for instruction and research. *Seismological Research Letters*, *84*(6), 1081–1088. https://doi.org/10.1785/0220110096

Heuret, A., Conrad, C. P., Funiciello, F., Lallemand, S., & Sandri, L. (2012). Relation between subduction megathrust earthquakes, trench sediment thickness and upper plate strain. *Geophysical Research Letters*, *39*(5), 1–6. https://doi.org/10.1029/2011GL050712

Heuret, A., Lallemand, S., Funiciello, F., Piromallo, C., & Faccenna, C. (2011). Physical characteristics of subduction interface type seismogenic zones revisited. *Geochemistry, Geophysics, Geosystems*, *12*(1), 1–26. https://doi.org/10.1029/2010gc003230

Hirauchi, K., Katayama, I., Uehara, S., Miyahara, M., & Takai, Y. (2010). Inhibition of subduction thrust earthquakes by low-temperature plastic flow in serpentine. *Earth and Planetary Science Letters*, *295*, 349–357. https://doi.org/10.1016/j.epsl.2010.04.007

Hirth, G., & Kohlstedt, D. L. (1996). Water in the oceanic upper mantle: Implications for rheology, melt extraction and the evolution of the lithosphere. *Earth and Planetary Science Letters*, *144*, 93–108. https://doi.org/10.1016/0012-821X(96)00154-9

Holtkamp, S. G., & Brudzinski, M. R. (2011). Earthquake swarms in circum-Pacific subduction zones. *Earth and Planetary Science Letters*, *305*, 215–225. https://doi.org/10.1016/j.epsl.2011.03.004

Horning, G., Canales, J. P., Carbotte, S. M., Han, S., Carton, H., Nedimović, M. R., & van Keken, P. E. (2016). A 2-D tomographic model of the Juan de Fuca plate from accretion at axial seamount to subduction at the Cascadia margin from an active source ocean bottom seismometer survey. *Journal of Geophysical Research: Solid Earth*, *121*(8), 5859–5879. https://doi.org/10.1002/2016JB013228

Hulme, S. M., Wheat, C. G., Fryer, P., & Mottl, M. J. (2010). Pore water chemistry of the Mariana serpentinite mud volcanoes: A window to the seismogenic zone. *Geochemistry, Geophysics, Geosystems*, *11*(1), 1–29. https://doi.org/10.1029/2009GC002674

Hyndman, R. D. (1979). Poisson's ratio in the oceanic crust—A review. *Tectonophysics*, *59*, 321–333. https://doi.org/10.1016/0040-1951(79)90053-2

Hyndman, R. D., Yamano, M., & Oleskevich, D. A. (1997). The seismogenic zone of subduction thrust faults. *The Island Arc*, *6*(3), 244–260. https://doi.org/10.1111/j.1440-1738.1997.tb00175.x

Ji, S., Li, A., Wang, Q., Long, C., Wang, H., Marcotte, D., & Salisbury, M. (2013). Seismic velocities, anisotropy, and shear-wave splitting of antigorite serpentinites and tectonic implications for subduction zones. *Journal of Geophysical Research: Solid Earth*, *118*(3), 1015–1037. https://doi.org/10.1002/jgrb.50110

Kandilarov, A., Mjelde, R., Flueh, E., & Pedersen, R. B. (2015). Vp/Vs-ratios and anisotropy on the northern Jan Mayen Ridge, North Atlantic, determined from ocean bottom seismic data. *Polar Science*, *9*(3), 293–310. https://doi.org/10.1016/j.polar.2015.06.001

Kato, T., Beavan, J., Matsushima, T., Kotake, Y., Camacho, J. T., & Nakao, S. (2003). Geodetic evidence of back-arc spreading in the Mariana Trough. *Geophysical Research Letters*, *30*(12). https://doi.org/10.1029/2002GL016757

Kelleher, J., & McCann, W. (1976). Buoyant zones, great earthquakes, and unstable boundaries of subduction. *Journal of Geophysical Research*, *81*(26), 4885–4896. https://doi.org/10.1029/JB081i026p04885

Kodaira, S., No, T., Nakamura, Y., Fujiwara, T., Kaiho, Y., Miura, S., et al. (2012). Coseismic fault rupture at the trench axis during the 2011 Tohoku-oki earthquake. *Nature Geoscience*, *5*, 646–650. https://doi.org/10.1038/ngeo1547

Kopp, H. (2013). Invited review paper: The control of subduction zone structural complexity and geometry on margin segmentation and seismicity. *Tectonophysics*, *589*, 1–16. https://doi.org/10.1016/j.tecto.2012.12.037

Kurz, J. H., Jahr, T., & Jentzsch, G. (2004). Earthquake swarm examples and a look at the generation mechanism of the Vogtland/Western Bohemia earthquake swarms. *Physics of the Earth and Planetary Interiors*, *142*(1–2), 75–88. https://doi.org/10.1016/j.pepi.2003.12.007

Lallemand, S., Peyret, M., van Rijsingen, E., Arcay, D., & Heuret, A. (2018). Roughness characteristics of oceanic seafloor prior to subduction in relation to the seismogenic potential of subduction zones. *Geochemistry, Geophysics, Geosystems*, *19*(7), 2121–2146. https://doi.org/10.1029/2018GC007434

Lauer, R. M., Saffer, D. M., & Harris, R. N. (2017). Links between clay transformation and earthquakes along the Costa Rican subduction margin. *Geophysical Research Letters*, *44*(15), 7725–7732. https://doi.org/10.1002/2017GL073744

Lay, T., Ammon, C. J., Kanamori, H., Xue, L., & Kim, M. J. (2011). Possible large near-trench slip during the 2011 Mw 9.0 off the Pacific coast of Tohoku Earthquake. Earth. *Planets and Space*, *63*, 687–692. https://doi.org/10.5047/eps.2011.05.033

Lefeldt, M., & Grevemeyer, I. (2008). Centroid depth and mechanism of trench-outer rise earthquakes. *Geophysical Journal International*, *172*(1), 240–251. https://doi.org/10.1111/j.1365-246X.2007.03616.x

Lefeldt, M., Grevemeyer, I., Goßler, J., & Bialas, J. (2009). Intraplate seismicity and related mantle hydration at the Nicaraguan trench outer rise. *Geophysical Journal International*, *178*, 742–752. https://doi.org/10.1111/j.1365-246X.2009.04167.x

Lefeldt, M., Ranero, C. R., & Grevemeyer, I. (2012). Seismic evidence of tectonic control on the depth of water influx into incoming oceanic plates at subduction trenches. *Geochemistry, Geophysics, Geosystems*, *13*(5). https://doi.org/10.1029/2012GC004043

Li, J., Shillington, D. J., Saffer, D. M., Bécel, A., Nedimović, M. R., Kuehn, H., et al. (2018). Connections between subducted sediment, pore-fluid pressure, and earthquake behavior along the Alaska megathrust. *Geology*, *46*(4), 299–302. https://doi.org/10.1130/g39557.1

Lomax, A., Virieux, J., Volant, P., & Berge-Thierry, C. (2000). Probabilistic earthquake location in 3D and layered models: Introduction of a Metropolis-Gibbs method and comparison with linear locations. In C. H. Thurber, & N. Rabinowitz (Eds.), *Advances in seismic event location* (pp. 101–134). Dordrecht, Nederlands: Springer Netherlands.

Marcaillou, B., Spence, G., Wang, K., Collot, J.-Y., & Ribodetti, A. (2008). Thermal segmentation along the N. Ecuador-S. Colombia margin (1-4°N): Prominent influence of sedimentation rate in the trench. *Earth and Planetary Science Letters*, *272*, 296–308. https://doi.org/10.1016/j.epsl.2008.04.049

Masson, D. G. (1991). Fault patterns at outer trench walls. *Marine Geophysical Researches*, *13*(3), 209–225. https://doi.org/10.1007/BF00369150

McKenzie, D., Jackson, J., & Priestley, K. (2005). Thermal structure of oceanic and continental lithosphere. *Earth and Planetary Science Letters*, *233*, 337–349. https://doi.org/10.1016/j.epsl.2005.02.005

Menapace, W., Tangunan, D., Maas, M., Williams, T., & Kopf, A. (2019). Rheology and biostratigraphy of the Mariana serpentine muds unravel mud volcano evolution. *Journal of Geophysical Research: Solid Earth*, *124*, 10752–10776. https://doi.org/10.1029/2019JB018265

Montagner, J.-P. (2007). Deep earth structure - Upper mantle structure: Global isotropic and anisotropic elastic tomography. In G. Schubert (Eds.), *Treatise on Geophysics* (Vol. 1, pp. 559–589). Amsterdam: Elsevier Science. https://doi.org/10.1016/B978-044452748-6.00018-3

Moore, J. C., & Saffer, D. (2001). Updip limit of the seismogenic zone beneath the accretionary prism of southwest Japan: An effect of diagenetic to low-grade metamorphic processes and increasing effective stress. *Geology*, *29*(2), 183–186. https://doi.org/10.1130/0091-7613(2001)029<0183:ULOTSZ>2.0.CO;2

Müller, R. D., Roest, W. R., Royer, J.-Y., Gahagan, L. M., & Sclater, J. G. (1997). Digital isochrons of the world's ocean floor. *Journal of Geophysical Research: Solid Earth*, *102*(B2), 3211–3214. https://doi.org/10.1029/96jb01781

Naif, S., Key, K., Constable, S., & Evans, R. L. (2015). Water-rich bending faults at the Middle America Trench. *Geochemistry, Geophysics, Geosystems*, *16*(8), https://doi.org/10.1002/2015GC005927.

Nakanishi, M., Tamaki, K., & Kobayashi, K. (1992). Magnetic anomaly lineations from Late Jurassic to Early Cretaceous in the west-central Pacific Ocean. *Geophysical Journal International*, *109*(3), 701–719. https://doi.org/10.1111/j.1365-246X.1992.tb00126.x

Oakley, A. J., Taylor, B., Fryer, P., Moore, G. F., Goodliffe, A. M., & Morgan, J. K. (2007). Emplacement, growth, and gravitational deformation of serpentinite seamounts on the Mariana forearc. *Geophysical Journal International*, *170*(2), 615–634. https://doi.org/10.1111/j.1365-246X.2007.03451.x

Oakley, A. J., Taylor, B., & Moore, G. F. (2008). Pacific Plate subduction beneath the central Mariana and Izu-Bonin fore arcs: New insights from an old margin. *Geochemistry, Geophysics, Geosystems*, *9*(6), 1–28. https://doi.org/10.1029/2007GC001820

Obana, K., Fujie, G., Takahashi, T., Yamamoto, Y., Nakamura, Y., Kodaira, S., et al. (2012). Normal-faulting earthquakes beneath the outer slope of the Japan Trench after the 2011 Tohoku earthquake: Implications for the stress regime in the incoming Pacific plate. *Geophysical Research Letters*, *39*(7). https://doi.org/10.1029/2011GL050399

Obana, K., Nakamura, Y., Fujie, G., Kodaira, S., Kaiho, Y., Yamamoto, Y., & Miura, S. (2018). Seismicity in the source areas of the 1896 and 1933 Sanriku earthquakes and implications for large near-trench earthquake faults. *Geophysical Journal International*, *212*(3), 2061–2072. https://doi.org/10.1093/gji/ggx532

Oleskevich, D. A., Hyndman, R. D., & Wang, K. (1999). The updip and downdip limits to great subduction earthquakes: Thermal and structural models of Cascadia, south Alaska, SW Japan, and Chile. *Journal of Geophysical Research*, *104*(B7), 14,965–14,991.

Pacheco, J. F., Sykes, L. R., & Scholz, C. H. (1993). Nature of seismic coupling along simple plate boundaries of the subduction type. *Journal of Geophysical Research*, *98*(B8), 14133–14159. https://doi.org/10.1029/93JB00349

Pavlis, G. L., Vernon, F., Harvey, D., & Quinlan, D. (2004). The generalized earthquake-location (GENLOC) package: An earthquake-location library. *Computers & Geosciences*, *30*(9–10), 1079–1091. https://doi.org/10.1016/j.cageo.2004.06.010

Podvin, P., & Lecomte, I. (1991). Finite difference computation of traveltimes in very contrasted velocity models: A massively parallel approach and its associated tools. *Geophysical Journal International*, *105*(1), 271–284. https://doi.org/10.1111/j.1365-246X.1991.tb03461.x

Pyle, M. L., Wiens, D. A., Weeraratne, D. S., Shore, P. J., Shiobara, H., & Sugioka, H. (2010). Shear velocity structure of the Mariana mantle wedge from Rayleigh wave phase velocities. *Journal of Geophysical Research: Solid Earth*, *115*(B11), 1–15. https://doi.org/10.1029/2009JB006976

Ranero, C. R., Grevemeyer, I., Sahling, H., Barckhausen, U., Hensen, C., Wallmann, K., et al. (2008). Hydrogeological system of erosional convergent margins and its influence on tectonics and interplate seismogenesis. *Geochemistry, Geophysics, Geosystems*, *9*(3). https://doi.org/10.1029/2007GC001679

Ranero, C. R., Phipps Morgan, J., McIntosh, K., & Reichert, C. (2003). Bending-related faulting and mantle serpentinization at the Middle America trench. *Nature*, *425*, 367–373. https://doi.org/10.1038/nature01961

Reynard, B. (2013). Serpentine in active subduction zones. *Lithos*, *178*, 171–185. https://doi.org/10.1016/j.lithos.2012.10.012

Rüpke, L. H., Phipps Morgan, J., Hort, M., & Connolly, J. A. D. (2004). Serpentine and the subduction zone water cycle. *Earth and Planetary Science Letters*, *223*(1–2), 17–34. https://doi.org/10.1016/j.epsl.2004.04.018

Saffer, D. M. (2017). Mapping fluids to subduction megathrust locking and slip behavior. *Geophysical Research Letters*, *44*, 9337–9340. https://doi.org/10.1002/2017GL075381

Saffer, D. M., & Marone, C. (2003). Comparison of smectite- and illite-rich gouge frictional properties: Application to the updip limit of the seismogenic zone along subduction megathrusts. *Earth and Planetary Science Letters*, *215*(1–2), 219–235. https://doi.org/10.1016/S0012-821X(03)00424-2

Saffer, D. M., & Tobin, H. J. (2011). Hydrogeology and mechanics of subduction zone forearcs: Fluid flow and pore pressure. *Annual Review of Earth and Planetary Sciences*, *39*, 157–186. https://doi.org/10.1146/annurev-earth-040610-133408

Salisbury, M. H., & Christensen, N. I. (1978). The seismic velocity structure of a traverse through the Bay of Islands Ophiolite Complex, Newfoundland, an exposure of oceanic crust and upper mantle. *Journal of Geophysical Research*, *83*(B2), 805–817. https://doi.org/10.1029/JB083iB02p00805

Scholz, C. H., & Campos, J. (2012). The seismic coupling of subduction zones revisited. *Journal of Geophysical Research*, *117*(B5), 1–22. https://doi.org/10.1029/2011JB009003

Scholz, J.-R., Barruol, G., Fontaine, F. R., Sigloch, K., Crawford, W. C., & Deen, M. (2017). Orienting ocean-bottom seismometers from *P*-wave and Rayleigh wave polarizations. *Geophysical Journal International*, *208*(3), 1277–1289. https://doi.org/10.1093/gji/ggw426

Seno, T. (2017). Subducted sediment thickness and Mw 9 earthquakes. *Journal of Geophysical Research: Solid Earth*, *122*(1), 470–491. https://doi.org/10.1002/2016JB013048

Shillington, D. J., Bécel, A., Nedimović, M. R., Kuehn, H., Webb, S. C., Abers, G. A., et al. (2015). Link between plate fabric, hydration and subduction zone seismicity in Alaska. *Nature Geoscience*, *8*, 961–964. https://doi.org/10.1038/ngeo2586

Shiobara, H., Sugioka, H., Mochizuki, K., Oki, S., Kanazawa, T., Fukao, Y., & Suyehiro, K. (2010). Double seismic zone in the North Mariana region revealed by long-term ocean bottom array observation. *Geophysical Journal International*, *183*(3), 1455–1469. https://doi.org/10.1111/j.1365-246X.2010.04799.x

Singh, S. C., Hananto, N., Mukti, M., Robinson, D. P., Das, S., Chauhan, A., et al. (2011). Aseismic zone and earthquake segmentation associated with a deep subducted seamount in Sumatra. *Nature Geoscience*, *4*, 308–311. https://doi.org/10.1038/ngeo1119

Snoke, J. A. (2003). FOCMEC: FOCal MEChanism Determinations. In W. H. K. Lee, H. Kanamori, P. C. Jennings, & C. Kisslinger (Eds.), *International Geophysics* (pp. 1629–1630). San Diego, CA: Acadmeic Press. https://doi.org/10.1016/S0074-6142(03)80291-7

Spinelli, G. A., & Saffer, D. M. (2004). Along-strike variations in underthrust sediment dewatering on the Nicoya margin, Costa Rica related to the updip limit of seismicity. *Geophysical Research Letters*, *31*(4), 1–5. https://doi.org/10.1029/2003GL018863

Stern, R. J., & Smoot, N. C. (1998). A bathymetric overview of the Mariana forearc. *The Island Arc*, *7*(3), 525–540. https://doi.org/10.1111/j.1440-1738.1998.00208.x

Takahashi, N., Kodaira, S., Tatsumi, Y., Kaneda, Y., & Suyehiro, K. (2008). Structure and growth of the Izu-Bonin-Mariana arc crust: 1. Seismic constraint on crust and mantle structure of the Mariana arc-back-arc system. *Journal of Geophysical Research*, *113*(B1), 1–18. https://doi.org/10.1029/2007JB005120

Tarantola, A. (1987). *Inverse problem theory: Methods for data fitting and model parameter estimation*. Amsterdam: Elsevier Science.

Tarantola, A., & Valette, B. (1982). Generalized nonlinear inverse problems solved using the least squares criterion. *Reviews of Geophysics and Space Physics*, *20*(2), 219–232. https://doi.org/10.1029/RG020i002p00219

Tibi, R., Wiens, D. A., & Yuan, X. (2008). Seismic evidence for widespread serpentinized forearc mantle along the Mariana convergence margin. *Geophysical Research Letters*, *35*(13), 1–6. https://doi.org/10.1029/2008GL034163

Tilmann, F. J., Grevemeyer, I., Flueh, E. R., Dahm, T., & Goßler, J. (2008). Seismicity in the outer rise offshore southern Chile: Indication of fluid effects in crust and mantle. *Earth and Planetary Science Letters*, *269*(1–2), 41–55. https://doi.org/10.1016/j.epsl.2008.01.044

Todd, E. K., Schwartz, S. Y., Mochizuki, K., Wallace, L. M., Sheehan, A. F., Webb, S. C., et al. (2018). Earthquakes and tremor linked to seamount subduction during shallow slow slip at the Hikurangi Margin, New Zealand. *Journal of Geophysical Research: Solid Earth*, *123*(8), 6769–6783. https://doi.org/10.1029/2018JB016136

Tréhu, A. M., Blakely, R. J., & Williams, M. C. (2012). Subducted seamounts and recent earthquakes beneath the central Cascadia forearc. *Geology*, *40*(2), 103–106. https://doi.org/10.1130/G32460.1

Ulmer, P., & Trommsdorff, V. (1995). Serpentine stability to mantle depths and subduction-related magmatism. *Science*, *268*(5212), 858–861. https://doi.org/10.1126/science.268.5212.858

Uyeda, S., & Kanamori, H. (1979). Back-arc opening and the mode of subduction. *Journal of Geophysical Research*, *84*(B3), 1049. https://doi.org/10.1029/JB084iB03p01049

van Keken, P. E., Hacker, B. R., Syracuse, E. M., & Abers, G. A. (2011). Subduction factory: 4. Depth-dependent flux of H2O from subducting slabs worldwide. *Journal of Geophysical Research: Solid Earth*, *116*(B1). https://doi.org/10.1029/2010JB007922

Vannucchi, P., Sage, F., Phipps Morgan, J., Remitti, F., & Collot, J.-Y. (2012). Toward a dynamic concept of the subduction channel at erosive convergent margins with implications for interplate material transfer. *Geochemistry Geophysics Geosystems*, *13*(1), 1–24. https://doi.org/10.1029/2011GC003846

Vrolijk, P. (1990). On the mechanical role of smectite in subduction zones. *Geology*, *18*(8), 703–707. https://doi.org/10.1130/0091-7613(1990)018<0703:OTMROS>2.3.CO;2

Waldhauser, F. (2001). *hypoDD—A program to compute double-difference hypocenter locations*. Menlo Park, CA: U.S. Geological Survey. https://doi.org/10.3133/ofr01113

Waldhauser, F., & Ellsworth, W. L. (2000). A double-difference earthquake location algorithm: Method and application to the Northern Hayward Fault, California. *Bulletin of the Seismological Society of America*, *90*(6), 1353–1368. https://doi.org/10.1785/0120000006

Wang, K., & Bilek, S. L. (2011). Do subducting seamounts generate or stop large earthquakes? *Geology*, *39*(9), 819–822. https://doi.org/10.1130/G31856.1

Wang, K., & Bilek, S. L. (2014). Invited review paper: Fault creep caused by subduction of rough seafloor relief. *Tectonophysics*, *610*, 1–24. https://doi.org/10.1016/j.tecto.2013.11.024

Watts, A. B. (2001). *Isostasy and flexure of the lithosphere*. Cambridge, UK: Cambridge University Press.

Yamashita, T. (1998). Simulation of seismicity due to fluid migration in a fault zone. *Geophysical Journal International*, *132*(3), 674–686. https://doi.org/10.1046/j.1365-246X.1998.00483.x

Yamashita, T. (1999). Pore creation due to fault slip in a fluid-permeated fault zone and its effect on seismicity: Generation mechanism of earthquake swarm. *Pure and Applied Geophysics*, *155*(2–4), 625–647. https://doi.org/10.1007/s000240050

Yang, H., Liu, Y., & Lin, J. (2012). Effects of subducted seamounts on megathrust earthquake nucleation and rupture propagation. *Geophysical Research Letters*, *39*(24), 1–6. https://doi.org/10.1029/2012GL053892

Yang, Y., & Forsyth, D. W. (2006). Regional tomographic inversion of the amplitude and phase of Rayleigh waves with 2-D sensitivity kernels. *Geophysical Journal International*, *166*(3), 1148–1160. https://doi.org/10.1111/j.1365-246X.2006.02972.x

Zhou, Z., & Lin, J. (2018). Elasto-plastic deformation and plate weakening due to normal faulting in the subducting plate along the Mariana Trench. *Tectonophysics*, *734–735*, 59–68. https://doi.org/10.1016/j.tecto.2018.04.008